Thin–Walled Structures 197 (2024) 111611

Contents lists available at ScienceDirect

Thin-Walled Structures

journal homepage: www.elsevier.com/locate/tws

Full length article

Comparison of two progressive damage models for predicting low-velocity impact behavior of woven composites

Yogesh Kumar [a,*], Mohammad Rezasefat [a], Sandro C. Amico [b], Andrea Manes [c], Patricia I. Dolez [d], James D. Hogan [a]

[a] Department of Mechanical Engineering, University of Alberta, Edmonton, AB T6G 2R3, Canada
[b] PPGE3M, Federal University of Rio Grande do Sul, Porto Alegre, 91501-970, Brazil
[c] Politecnico di Milano, Dipartimento di Meccanica, via La Masa 1, Milano 20155, Italy
[d] Department of Human Ecology, University of Alberta, Edmonton, AB T6G 2R3, Canada

ARTICLE INFO

Keywords:
Woven composites
Low-velocity impact
Strain-rate dependency
Interlaminar and intralaminar failure
Non-physical parameters
LS-Dyna

ABSTRACT

This research focuses on comparing the two progressive damage models available in the explicit nonlinear finite element software LS-Dyna. To explore the prediction capabilities in terms of mechanical response and dominating failure modes in S2 glass woven composites, low velocity impact response at four different energies ranging from 27.9 J to 109.7 J were considered in this study. A macro-homogeneous solid element formulated finite element model was simulated to understand the response and failure mechanics in the laminate under low-velocity impact. The material modeling was carried out utilizing the MAT 55 and MAT 162 material models. An effort has been made for robust calibration of the various physical and non-physical parameters in both material cards for accurate predictions. The prediction capabilities of the models were then examined by comparing them against the experimental results, which fall within the deviation of ~11%. The results show that MAT 162 yields a better resemblance with the damage morphology patterns and the delamination for the accounted impact zone, due to inclusion of strain-rate effect. Overall, this paper provides insight into the limitations and advantages of both material models, which establishes the route for the selection of the appropriate material model for simulating impact behavior in woven composites.

1. Introduction

Woven composites have been proven to have superior performance when compared to conventional composite materials in domains like Defence, Aerospace, and Automotives [1–4]. The application of these advanced materials includes energy absorption, impact resistance, ballistic performance, and high structural strength and stiffness [5–7]. Researchers have explored the performance of different kinds of unidirectional and woven composites subjected to different loading conditions via experiments, numerical modeling, and analytical methods [8–11]. For example, Shah et al. [12] studied the impact performance of thermoplastic and thermoset E-glass woven composites. They concluded that thermoplastic-based composites requires higher magnitude of impact energy for damage transition, resulting in higher fracture toughness and crack resistance when loaded with single and recurring drop tower impacts. Similarly, there are many experimental studies published over the past few decades involving a variety of different setups to characterize the material and understand the damage mechanisms of the composite materials [13–16]. Cheng et al. [17, 18] extensively explored plain-weave composites under low velocity impacts, followed by compression-after impact, tension-after impact, and fatigue response of the degraded laminate. The results depicted that the low-velocity impacts cause a high degradation effect, and the post-impact damage propagation is significantly dependent on the load sequence in the fatigue testing. The proposed numerical model incorporates Hashin's failure criteria for the various damage modes and cohesive zone model for the interlaminar failure within the composite laminate. Delamination, debonding, matrix failure, and fiber breakage are the failure or damage modes that manifest in the composite panels when experiencing low-velocity impacts (LVI) [19–22]. Delamination is considered one of the most crucial damages for the impacted composites, as driven by matrix cracking, bending cracks, and shear cracks [23,24]. Based on previous studies [25,26] which made an attempt towards quantifying the delamination in woven and hybrid composites, the damage modes get influenced by the impact parameters including the shape and mass of the impactor. Permanent indentation is another phenomenon that occurs in composites under

* Corresponding author.
E-mail address: yogesh.kumar@ualberta.ca (Y. Kumar).

https://doi.org/10.1016/j.tws.2024.111611
Received 23 October 2023; Received in revised form 29 December 2023; Accepted 17 January 2024
Available online 19 January 2024
0263-8231/© 2024 The Author(s). Published by Elsevier Ltd. This is an open access article under the CC BY-NC-ND license (http://creativecommons.org/licenses/by-nc-nd/4.0/).

Nomenclature

List of Abbreviations & Notations

ALPH	Shear stress parameter for the nonlinear term
AM1/AM2, AM3, AM4	Coefficients for strain-rate softening
AMODEL	Option to define the material model based on architecture of the laminate: EQ1 = Unidirectional or EQ2 = Fabric laminate
AOPT	Material axes defining option
BETA	Shear weighting factor to be used in fiber tensile mode
CDM	Continuum damage model
CFRP	Carbon fiber reinforced polymer
DFAILM	Maximum strain for matrix straining in tension or compression
DFAILS, DFAILT, DFAILC	Maximum strains for failure of laminate in shear, tension and compression
ECRSH	Limit compressive volume strain for element eroding
EEXPN	Limit tensile volume strain for element eroding
EFS	Effective failure strain
ELFORM 1	Element formulation: Constant stress solid element
ELIMIT	Element eroding axial strain parameter
FBRT	Softening parameter for fiber tensile strength
FEM	Finite element method
LVI	Low-velocity impact
MAT 162	Composite MSC damage model
MAT 54/55	Enhanced composite damage model
PARAM	Exponent term in the damage model for the tie-break constraint
PHIC	Mohr-column friction parameter for contact definition
QM	Coefficient for hourglass energy
SDELM	Scale factor for delamination criterion
SLIMT1	Minimum stress limit factor for fiber tension failure
SOFT	Crashfront reduction softening parameter
YCFAC	Softening parameter for fiber compressive strength

Notations used in MAT 55 material model description

β	Shear weighting factor
$\nu_{ba,ab}$	Poisson's ratio
σ_{aa}, σ_{bb}	Stress in longitudinal and transverse direction
σ_{ab}	Shear stress
E_a, E_b	Elastic modulus in longitudinal and transverse direction
e_f^2, e_c^2	Failure of the fibers under tension and compression
e_{md}^2	Failure of the matrix under tension and compression
G_{ab}	Shear modulus in ab plane
S_c	In-plane shear strength
X_t, Y_t	Longitudinal and transverse tensile strength
X_c, Y_c	Longitudinal and transverse compressive strength
$X_{t'}$, $X_{c'}$	Reduced longitudinal tensile and compressive strength

Notations used in MAT 162 material model description

σ_a, σ_b, σ_c	Stress in longitudinal, transverse and through-thickness direction
τ_{ab}, τ_{ca}, τ_{bc}	Shear stress in ab, ca and bc plane
C_{rate1}, C_{rate2}, C_{rate3}, C_{rate4}	Coefficients for strain-rate dependency
m_j	Coefficient for strain rate softening parameters
r_j	Damage threshold
S_{ab}, S_{bc}, S_{ca}	Matrix mode shear strength in ab, bc and ca plane
S_{aC}, S_{bC}	Longitudinal and transverse compressive strength
S_{aFS}, S_{bFS}	Shear strength in longitudinal and transverse direction
S_{aT}, S_{bT}, S_{cT}	Longitudinal, transverse and through-thickness tensile strength
S_{delam}	Scale factor for delamination criteria
S_{FC}	Crush shear strength
X_0	Quasi-static strain-rate property for the reference
X_{RT}	Strain-rate dependent property at the average strain rate
$\dot{\bar{\varepsilon}}_0$	Average strain rate

low-velocity impacts. This localized deformation is mainly due to the anisotropic material properties which are influenced by the material non-linearities from fiber orientation and matrix characteristics [27–29]. Mitrevski et al. [30,31] summarized the influence of the impactor shape at various low-ranged energies on the delamination propagation and mechanical response in the carbon/epxoy laminate, examined through non-destructive inspection techniques. But experiments restrict us to get full insights due to limitations on resources, and access to harsh conditions, but most importantly challenges related to the examination of the internal behavioral patterns such as interfacial properties between two constituents in a material.

In comparison to the expensive and laborious experimental procedure, the finite element method (FEM) is acknowledged as an extremely realistic and effective method for simulating and predicting the complex damage behavior of woven fiber composite laminates under impact loads [32]. As a result, the FEM has been widely used to investigate the impact damage behavior of composite laminates [33–35]. In their study, Yang et al. [36] proposed a finite element model for the low-velocity impact (LVI) and compression-after impact (CAI) on woven carbon fiber/epoxy composites. The model predicted a good response of the laminate subjected to different impactor diameters and energies when compared to experiments. More localized damage was observed with the impactor of lower diameter. However, the failure and buckling modes remained almost unaffected by the change in impactor size. Rajaneesh et al. [37] also conducted an investigation of LVI-CAI tests using the ply-scaled finite element model that has quasi-isotropic composite stacking. They improved delay damage parameters from the previous study [38] and incorporated in-situ strengths, plasticity, and nonlinear damage of the ply. The proposed model by Rajaneesh

et al. [37] lacks an estimation of the transverse compression failure mode and the directionality in the delamination propagation in the composite. In some other studies, researchers have also focused on the energy dissipation mechanisms [39], different shapes of the laminate (eg. elliptic curved composite structures) [40,41], and hybridization of the composites [42]. Haibao et al. [26] experimentally and numerically investigated a hybrid unidirectional/woven composite laminate under impact loading up to 25 J energy. They noted that the stacking sequence in the material can affect the impact response of the composite by altering the stiffness of the laminate. The observed dominating failure modes include delamination and matrix cracking which are the result of the 90° plies. In addition, damage resistance improved with the allotment of woven plies as the top and bottom layers in the material system. Regarding hybridization of composite panels, many research teams have evaluated different combinations, including S2 glass/aramid [32], carbon fiber/UHMWPE [43,44] and carbon/glass/basalt fibers based woven composites [45]. In the study done by Choi et al. [46], the authors developed a shell element-based predictive model using the user-defined subroutine incorporating strain-based failure theory to achieve more economic and improved accuracy for low-velocity impact loading scenarios. The efficiency of the model was confirmed by comparing it with experiment results and other FEM models (i.e., MAT 22 and MAT 54 material models from the LS-Dyna directory). Such shell-element-based models are incapable of predicting the interaction of each ply within the composite laminate which plays a crucial role and helps in determining the failure response of the component under the loading scenario. Over the past decade, different composites were studied under a variety of impact loadings and using numerical models, but assuming a general static algorithm, hence disregarding strain-rate dependent properties [47–50]. Liao et al. [51] developed a VUMAT code for consideration of the damage model including plastic strain rate, along with a bi-linear cohesive zone model applicable to out-of-plane impact loading. Another study performed by Wang et al. [48] incorporated the strain-rate dependent damage model based on the Yen–Caiazoo function [52] which includes the approximation of strength and stiffness across various strain-rates. This study covers the impact energies range from 5 J to 10 J only, on the carbon-fiber unidirectional composite. They found a substantially increasing strain-rate effect on inter- and intralaminar damage evolution and contact force history output at higher impact energies.

One of the most challenging parts of nonlinear finite element modeling lies in the calibration and optimization of the material models with the non-physical inputs to capture the actual damage morphology of the composite in these physics-driven simulations [53–56]. In the LS-Dyna software (commercial explicit finite element solver), the directory contains different material models (e.g., MAT 22 [57], MAT 54/55 [55], MAT 58 [58], MAT 81 [59], MAT 161/162 [60] and MAT 219 [61]) for composites based on the compatibility of element types, nature of the material, and damage models and failure modes [62,63]. Especially, the MAT 54/55 material model has been extensively used in the application of crushing simulation, especially for axial loading, as reported by Sun et al. [64] but relatively fewer studies have been conducted for impact applications [62,65–73]. Sun et al. [64] summarized the norms researchers have been using for the calibration of progressive failure model parameters (21 physical and 6 non-physical, in the case of MAT 54/55) and compared them with other existing modeling strategies (including tie-break method for inter-laminar failure investigation) within LS-Dyna as well as other commercial FE packages (e.g., ABAQUS and PAM CRASH). For instance, Rossi et al. [62] compared five different LS-Dyna constitutive models (MAT 22, MAT 54, MAT 55, MAT 58, and MAT 59) for effectiveness and applicability for the pendulum-based LVI at 5 J and 10 J energies experienced by unidirectional carbon fiber reinforced polymer (CFRP) composite IM7/8552. After the in-depth parametric studies as performed by other authors [55,74], only MAT 55 (progressive damage model) and MAT 59 (continuum damage model) were able to accurately characterize the damage area and shape in both quantitative and qualitative aspects for the considered energy cases. They also pointed out the significant effect of failure strain parameters *(DFAILs)* in the MAT 54/55 models toward energy dissipation. In another study [72], Ao et al. proposed a novel 3D CDM model for the impact response of woven CFRP composites with intralaminar damage evolution in the LS-Dyna environment using user-defined subroutines and compared it with other existing material models (i.e., MAT 54 and MAT 58). The comparative study was done based on tensile simulation to understand the effectiveness of the proposed CDM model, and then the validated model was used to simulate four different LVI tests at different stacking sequences. In qualitative and quantitative manners, the model showed a good agreement with the experiments in terms of Force–time, Energy–time plots (2% deviation), and delamination areas (5% deviation). Similar to this, some authors also study different material models in FE software ABAQUS using VUMATs to evaluate the effectiveness of the formulation towards predicting the failure mechanisms, delamination, and global mechanical response (i.e., peak force, peak displacement, and dissipated energy) [29,70]. Recently, Sridharan et al. [69] compared the MAT 162 material model from LS-Dyna and VUMAT subroutine-based progressive damage models for low-velocity and high-velocity impact on S2 glass composite. MAT 162 depicts more resemblance with the experimental values in case of high-velocity impacts, while due to hour-glassing, its prediction performance reduces for the low-velocity case and is reported to be subjective to the thickness of the laminate. As a result, the ABAQUS VUMAT model has been found to lack the ability to estimate the through-the-thickness crush response, hence reducing the efficiency of the model for high-velocity impacts. These studies provide insight into the selection of appropriate material models, modeling approach, incorporated failure modes, estimation of computational cost, and complexity of the model towards implementation (calibration & optimization) to the scientific community and industries for more robust prediction of the behavior of composite materials; we seek to contribute to these efforts in this paper.

Many researchers have not considered the strain-rate effect as they tend to focus on a narrow range of impact energies and validate their models specific to those impact energies. In such cases, the strain rate effect might not be significantly variable within that narrow band, leading to reasonable accuracy in simulation results even without explicitly considering strain-rate effects. In our work, we aim to establish a model that can cover a wide range of impact energies, from low (27.9 J) to perforation (109.7 J) levels. This broader scope necessitates a more detailed consideration of strain-rate effects, as they can vary significantly across different impact energy levels. In this study, we first performed experiments to investigate the performance of the S2 glass fiber reinforced polymer composite for LVI using the drop-tower apparatus with post-mortem investigation on the delamination and damage morphology using the backlight technique. Second, two macro-homogeneous finite element models have been developed focusing on the estimation of inter/intra-laminar failure modes in the composite and understanding the influence of various non-physical parameters used in material models (MAT 55 and MAT 162) and their parametric study. This comparative study had been conducted to analyze the effect of the most important and influential non-physical parameters in progressive damage models with and without strain-rate dependency.

2. Material properties and experiments

2.1. Material description

The woven glass fiber laminates of this work were formerly characterized in [71,75]. Hexcel®8-harness satin S2 glass (302 g/m^2, 0.24 mm, 22 threads per cm- https://www.hexcel.com) fabrics were used as reinforcement. Epoxy resin AR260 with AH260 hardener (AR/AH260) – 100/26 g/g ratio, supplied by the Barracuda Advanced

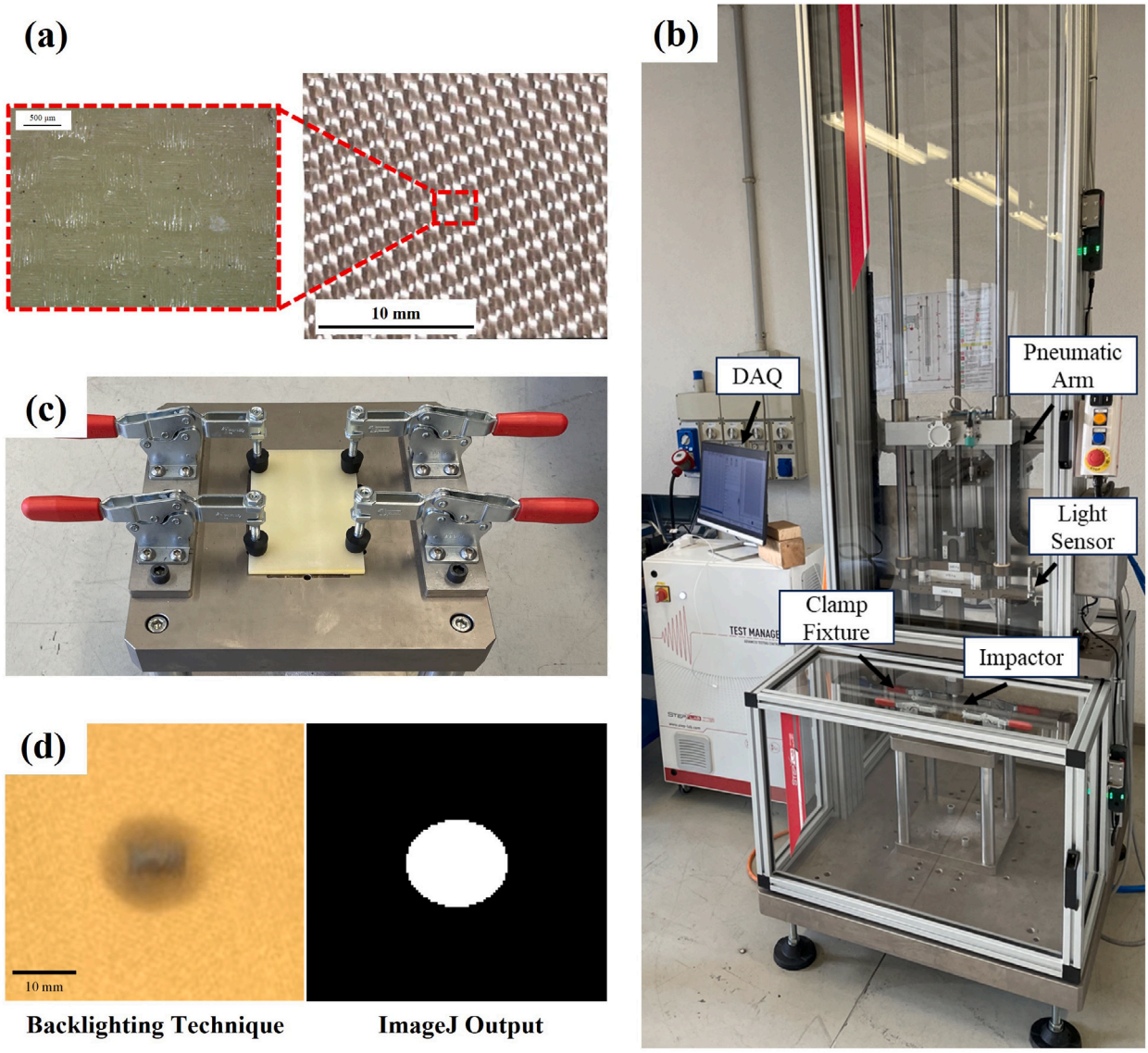

Fig. 1. Summary of the experimental setup for the low-velocity impact testing according to the ASTM D7136 standard: (a) architecture of the woven S2 glass fabric, (b) The drop-tower impact machine with the hemispherical striker, (c) The fixture used to clamp the specimen during the tests, and (d) the damaged specimen and the damage counter after processed in the ImageJ software.

Composites (www.barracudacomposites.com.br), was used to manufacture the laminates by vacuum infusion as summarized by Silva et al. in [76]. Dry fabrics (16 layers), (630 × 320) mm, were stacked on the one-sided mold which included eight warp and eight weft layers with a sequence of $[0°/90°]_8$, a layer of peel ply, and the flow mesh was placed on top covering the entire molding area, to aid resin lateral distribution. Inlet and outlet gates (distribution channels) were positioned on the mold, which was sealed using tacky tape at the periphery of the molding area, followed by a vacuum bag. The cavity was evacuated, removing air, and compacting the reinforcement. Resin enters the sealed cavity via the inlet due to the imposed vacuum (100 kPa), infiltrating the stack of layers. After infiltration, the material was cured for 24 h under a vacuum, and the composite was extracted and subjected to post-curing (16 h at 65 °C). The 4-mm thick final laminates were analyzed using C-scan ultrasonic inspection (NDT Systems equipment, Raptor model), with 2.25 MHz (0.5 inches) transducer and water as a coupling medium. The resin was considered to be suitably distributed throughout the composite, as described in previous works [75,76]. The laminate presented good homogeneity, with a uniform distribution of resin on the molded area. Specimens for the low-velocity impact tests were obtained by water jet cutting.

2.2. Low-velocity impact test

Low-velocity impact tests were performed according to ASTM D7136 standard with a drop weight impact tower. The (150 × 100) mm specimens, with an areal density of 6.96 kg/m^2, were impacted with a hemispherical impactor of 16 mm diameter. An optical sensor was used to measure the impact velocity of the impactor at the onset of impact with the laminate and the contact force between the specimen and impactor was acquired with a load cell. An energy profiling diagram [77] was used to assess the impact response of GFRP laminates and four specific energies were selected for a detailed study to develop models applicable across various energy ranges. A range of impact energies of 27.9 J to 109.7 J was studied by varying the impactor mass (5.66 or 15.58 kg) and height (360 to 1440 mm), see Table 1. The specimen was fixed on a rigid plate with a (125×75) mm free rectangular area using four fixtures equipped with rubber dampers according to the cited standard (see Fig. 1c). Each test was repeated twice to validate the repeatability of the experimental observations. The impact system is equipped with a pneumatic arm to prevent unwanted multiple hits on the specimen. The GFRP composite was previously characterized in [71,

Table 1
Summary of the drop-weight impact tests.

Test number	Mass (kg)	Impact velocity (m/s)	Impact energy (J)
1	5.66	3.13	27.8
2	5.66	3.14	27.9
3	5.66	3.98	44.8
4	5.66	4.02	45.8
5	5.66	5.02	71.3
6	5.66	5.09	73.2
7	15.58	3.76	109.7
8	15.58	3.75	109.7

Table 2
Physical material properties obtained from various standardized tests of the laminate and interface properties used for delamination [71,75,79–81].

Properties	Symbol [Unit]	Value
S2 Glass Woven Composite Laminate		
Density	ρ [kg/m^3]	1740
Initial modulus	E_a, E_b [GPa]	36.50
Elastic modulus	E_c [GPa]	11.80
Poisson's ratio	υ_{ba}	0.12
Poisson's ratio	υ_{ca}, υ_{cb}	0.18
Shear modulus	G_{ab} [GPa]	1.81
Shear modulus	G_{cb}, G_{ca} [GPa]	2.14
Longitudinal tensile strength	X_t [MPa]	482.80
Longitudinal compressive strength	X_c [MPa]	333.25
Transverse tensile strength	Y_t [MPa]	482.80
Transverse compressive strength	Y_c [MPa]	337.30
In-plane shear strength	S_c [MPa]	82
Crush shear strength[a]	S_{crush} [MPa]	58
Interface Properties for Delamination		
Strength	N [MPa]	45.90
	S [MPa]	49.50
Fracture toughness	G_n^c [N/mm]	0.98
	G_s^c [N/mm]	3.71

[a] Only employed in MAT 162 material model.

75], and the inputs for the damage models were used accordingly. For the input values that were unavailable from mechanical tests, material properties for similar GFRP composites from the referenced literature were used, as summarized in Table 2.

The backlighting technique was used to measure the impacted damaged area and delamination in the impacted composite samples. This method is effective in investigating the damage in GFRP specimens due to the reduction in translucency induced by damage [8,78]. For that, the damaged specimen is placed in a fixture with a light source, and high-resolution images are taken and later processed with ImageJ software [26] to estimate the total damaged area.

3. Finite element modeling

A 3D finite element (FE) model of the 16-layer laminate was simulated in the LS-Dyna explicit solver environment based on the solid elements *(ELFORM 1)*, which are constant-stress solid elements compatible with hourglass controlling. Due to the symmetry condition, only a quarter of the laminate (dimension: 75×50 mm) was simulated. The experimental boundary condition was implemented using a fixed rigid clamp at the back surface of the laminate (in relation to the impact). To represent the rubber fixture used in the experimental setup to avoid out-of-plane movement of the laminate, the nodes at corners were constrained. A region of fine mesh was defined near the impactor/laminate contact zone with an element size of 1×1 mm. Far from the contact zone, a coarser mesh was defined with an element size of 5×5 mm to reduce computational time. In the simulation, the rigid impactor, 16 mm in diameter, impacted the laminate with initial impact energy as measured for each experiment, as summarized in Table 2, and was constrained to have translation motion in the Z-direction only as to avoid any out-of-plane movement. Fig. 2 shows the schematic for the numerical model developed for this study.

The interaction between the plies of the laminate was defined based on tiebreak contact definition using the *AUTOMATIC ONE WAY SURFACE TO SURFACE TIEBREAK* option. The interaction response formulation in the FE model uses Option 9: Discrete Crack Model with the Benzeggagh–Kenane (B–K) law by assigning a negative value to the *PARAM* parameter in the contact definition card, as defined in the LS-Dyna documentation [82]. It also includes the quadratic mixed mode delamination criterion and a damage formulation [82,83]. The interaction between different plies after intralaminar failure was considered by defining a penalty-based general contact algorithm between adjacent layers which had a friction coefficient of 0.5 [84] with normal and tangential stiffness for contact stability [81]. The *AUTOMATIC SURFACE TO SURFACE* contact definition was defined between the bottom-placed rigid clamps and laminate and the impactor for more accurately modeling the physical state. The static and dynamic coefficients of friction were set to 0.3 in both interactions [85]. To make the simulation model more stabilized, some parameters from the *CONTROL CONTACT* cards were also invoked. Contact surface maximum penetration check multiplier with magnitude 4 was deployed to terminate the simulation after reaching the criteria. Sliding interface penalties were also turned on with a default value of 0.1. A detailed description of the contact formulation has been provided in Appendix A3.

Zero-energy modes (also known as hourglass modes) are a phenomenon induced in the FE models due to the use of under-integrated element formulation (such as *ELFORM 1*) which provides zero-strain and stress values and will apparently lead to inaccurate force–time response and excessive element distortion [69,86]. Moin et al. [87] and Rajaneesh et al. [37] have demonstrated the effectiveness of stiffness-based hourglass formulation (Type 4 and 5) for the low-velocity impact testing of composite materials. In this study, we have used Type 5: Flanagan–Belytschko stiffness form with exact volume integration formulation [88] and investigated the influence of the coefficient of the hourglass *(QM)* in terms of hourglass energy and force–displacement response to reduce the artificial energy and stiffness within 10%, as recommended in [87].

4. Description of material models

As mentioned earlier, LS-Dyna provided a variety of different material models describing the behavior of laminated composite materials [62,64,74]. This study focuses on a comprehensive study of the prediction capabilities of two material models, i.e., MAT 55 *(ENHANCED COMPOSITE DAMAGE)* and MAT 162 *(COMPOSITE MSC)* progressive damage models. Table 3 depicts the comparison of these aforementioned material models and the detailed formulation of both material models has been provided in Appendix A.

MAT 54/55 is a well-known progressive damage material model used for modeling composite materials. The model has two options for failure theories: Chang-Chang failure criteria (MAT 54) and Tsai–Wu failure criteria (MAT 55). There are numerous studies based on the MAT 54 having solely Chang-Chang failure criteria [54,55,64,69], but only a limited number of studies have been carried out based on MAT 55 failure criteria (Tsai–Wu) when subjected to drop-tower-based low-velocity impact [68,89]. With MAT 55 material card, the modes of the tensile and compressive fiber are driven as in the Chang-Chang criteria [90], and the tensile and compressive matrix failure are defined by the Tsai–Wu criteria [91]. The failure criteria in both fiber and matrix rupture by tension are influenced by *BETA*, a shear weighting factor defined in the material model. The prediction accuracy of MAT 55 is particularly sensitive to changes in non-physical constitutive parameters and which cannot be determined by experimental means. Many researchers have studied the significance of calibrating these non-physical parameters subjected to variety of loading conditions [55,68,73,92]. Camargo et al. [93] reported the inter-dependency of these

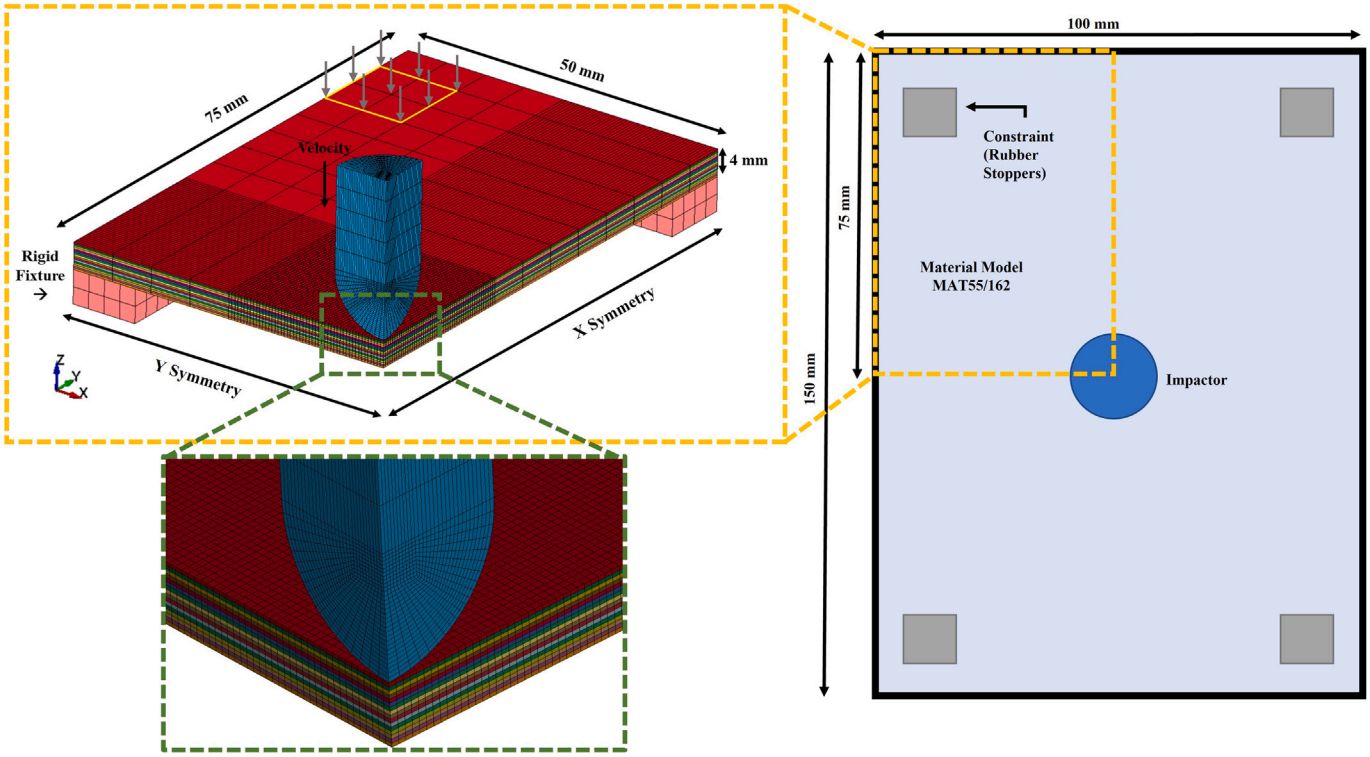

Fig. 2. Schematic of the quarter model used for simulating the low-velocity impact response of the S2 glass woven laminate composite according to the ASTM D7136 standard. The schematic highlights the boundary conditions applied on the edges of the model. X and Y symmetry was applied to replicate the full model setup, and the outer edges were constrained as per the actual experimental setup to eliminate the unwanted oscillations in the model. A more refined mesh region has been used in the impact zone to better capture the physics and failure features in the model.

Table 3
Comparison of the material models: MAT 55 and MAT 162.

	MAT 55	MAT 162
Title	Enhanced composite damage	Composite MSC
Element type	Solid Shell Thick shell	Solid
Non-linear shear behavior	Yes	No
Failure modes	Five stress-based criteria: Tensile fiber failure Compressive fiber failure Tensile matrix failure Compressive matrix failure Maximum stress	Six strain-based criteria: Tensile fiber failure Compressive fiber failure Perpendicular matrix failure Parallel matrix failure Fiber crush failure mode Delamination mode
Integrated delamination criteria	No	Yes
Progressive failure model	No post-peak softening	Exponential strain softening law
Element erosion criteria	Effective failure strain	Effective failure strain Limit for compressive volume strain Limit for tensile volume strain
Strain-rate dependency	No	Yes

parameters for capturing the failure mechanisms from impacts. Another material model considered in this study was the MAT 162 which is governed by Hashin failure [94] criteria and post-damage softening suggested by Matzenmiller et al. [95]. Both of these material models have the ability to define the material directional axes using the *AOPT* option, but only MAT 162 has a distinct formulation to model the unidirectional laminate as well as woven laminate, as toggled by using *AMODEL* option in the material card. In the fabric model of the MAT 162, the element can be removed if it exceeds the fiber tensile failure in both in-plane directions predicted in the element and the axial tensile strain is greater than the defined *ELIMIT* (Element eroding axial strain term). In other cases, the element will be eroded, if the tensile or compressive relative volume in a failed element is greater than or less than *EEXPN* (Limit tensile relative volume term) and *ECRSH* (Limit compressive relative volume term), respectively [96]. The material card definition has four softening parameters abbreviated as *AM* to control the failure modes in corresponding directions. One of the advantages of using the MAT 162 material model is that it does not require extensive cohesive zone modeling for the estimation of delamination and an additional scale factor for the same is provided, known as the *SDELM* (scale factor for delamination criteria) [73]. This material card also allows the use of the strain-rate effect on the mechanical properties. There are a total of four coefficients of strain-rate parameters C_{rates}, for strength values, shear moduli, transverse moduli, and the in-plane

Table 4
Parameters definition used in the material models [60,79,97,98].

	Property	Symbol	Value
MAT 55	Effective failure strain[a]	EFS	0.28
	Shear stress parameter for the nonlinear term	ALPH	0.45
	Crashfront reduction softening parameter[a]	SOFT	0.35
	Softening parameter for fiber tensile strength	FBRT	0.35
	Softening parameter for fiber compressive strength	YCFAC	2.25
MAT 162	Element eroding axial strain parameter[a]	ELIMIT	0.25
	Scale factor for delamination criterion	SDELM	1.2
	Limit compressive volume strain for element eroding	ECRSH	0.001
	Limit tensile volume strain for element eroding	EEXPN	1.1
	Coefficient for strain-rate dependent strength[a]	C_{rate1}	0.045
	Coefficient for strain-rate dependent axial moduli[a]	C_{rate2}	0.034
	Coefficient for strain-rate dependent shear moduli[a]	C_{rate3}	0.0
	Coefficient for strain-rate dependent transverse moduli[a]	C_{rate4}	0.048
	Coefficient for strain-rate softening for fiber damage[a]	AM1/AM2	0.0001
	Coefficient for strain-rate softening for fiber crush and punch shear damage[a]	AM3	0.4
	Coefficient for strain-rate softening for matrix damage[a]	AM4	0.2

[a] Parametric study presented in this research.

elastic moduli. Few studies have been done on understanding the effect of these parameters in high-velocity impacts [79]. An attempt has been made here to evaluate these parameters for low-velocity impacts and their physical significance on the damage prediction in different modes. In Table 4, the parameters from both material models used in this study have been summarized. Due to much literature data available on the MAT 54/55 material model, some parameters are well established in the literature and can be directly considered in the development of numerical models [68,79,93,97,98]. This was the case for ALPH, FBRT and YCFAC for the simulations carried out in this work. The SDELM parameter from the MAT 162 model has also been well-established for low-velocity impact [23,71,73,99]. For relevant comparison between the material models, ELIMIT (strain-based element erosion) was chosen as the driving parameter to control the element erosion under the impact. The consistent and well-established values of the parameters can be utilized due to similarity between the present material and the materials described in the literature [77,97,100,101].

5. Results and discussion

In this section, the mechanical response of the laminate under different low-velocity impact energies are first discussed Section 5.1 along with the experimental results for the validation of the developed numerical models, in terms of force–time, force–displacement, and energy–time plots. Secondly in Section 5.2, the damage morphology and the delamination initiating and propagating along the different impact energies are illustrated in detail with comments provided on inter-laminar and intra-laminar failure modes. Thirdly 5.3, the parametric study on the influential non-physical parameters involved in both the selected material models in this study is reported.

5.1. Force–time, force–displacement and energy–time response

This subsection describes the low-velocity impact response obtained through both the material models and compared with the experimental results based on the force–time, force–displacement, and energy–time curves. To understand the behavior of the material at different damage limits, we considered two energies (27.9 J and 45.8 J) at which the impactor is rebounding back after impacting the laminate. To cover the penetration and perforation limits of the laminate, 72.0 J and 109.7 J energy cases were also included in this study. Figs. 3a–d and Figs. 4a–d show the force–time and force–displacement estimations for all four energies considered in this study. Similarly, Fig. 5 depicts the generation and dissipation of the energy for all the cases. The plots show a comparison between the history outputs from both the numerical models and the experimental study. In general, the mechanical response predicted by both the material models in all the energy cases shows a good resemblance with the experimental data, especially for the ascending part of the curve i.e., before reaching the peak force. The post-damage response varies with the change in impact energy and the employed material models, as further discussed in this section.

Higher energy impacts cultivates more complex mechanical behavior and more features than lower energy cases due to the initiation and propagation of damage through the laminate [69,71,102,103]. The proposed models accounts for them, and the prediction capabilities improve with the increase in the impact energy. Relatively smooth curves were obtained for the lowest energy (27.9 J), due to the neglectable state of damage experienced by the laminate in this case. In the case of 45.8 J, the force profile after reaching the maximum, drops and then again reverts back, this attributes towards the breakage of fibers in some layers but not penetrating through completely, as manifested in Fig. 3b. For the higher energies, the sudden drop in the force values symbolizes the aggressive failure of the material. Post fiber failure, high oscillations in the numerical predictions are encountered at higher energies due to the flexural vibration experienced by the laminate during impact. The major difference between the material models can be seen through the prediction made for the later part of the curves. Most notably, the minor and major force drops were also captured by the FE solution which is attributed to accurate prediction of the progressive damage during the impact event. Post-softening mechanics for both the numerical models are driven by different theories as explained earlier in Section 4 and Appendix A. In terms of the impact time duration, the MAT 162 material model outperforms the MAT 55. Based on MAT 55, models have an error of 23.26% and 26.62% for the 45.8 J and 72.0 J energies, whereas MAT 162 predicts better results with only −3.07% and −2.95% of error for the same energies. In the case of perforation energy of 109.7 J, a similar trend of early failure prediction can be observed by the MAT 55 model.

From Fig. 4, the portion of force–displacement curves before reaching the peak force at each of the energies demonstrates the impact bending stiffness of the laminate [103,104]. At the rebounding energies (27.9 and 45.8 J), MAT 55 slightly overestimates the experimental results with a higher slope value. For the highest energy, the open curve for the force–displacement as shown in Fig. 4d symbolizes the penetration of the impactor through all the plies of the laminate [32]. The rate-dependent progressive damage model goes through capturing all the damage constituents over the impact time. The instantaneous drop in the force value at 12 msec shows the inefficiency of the artificial non-physical post-softening behavior. In Fig. 5, the plotted energy–time curve shows the comparison of both numerical models with the experiments. MAT 162 model demonstrates good agreement with the generation of energy during the impact duration, especially in the case of 72.0 J and 109.7 J. For the lower energy cases (27.9 J and 45.8 J), MAT 55 performs better in terms of energy generation since, these

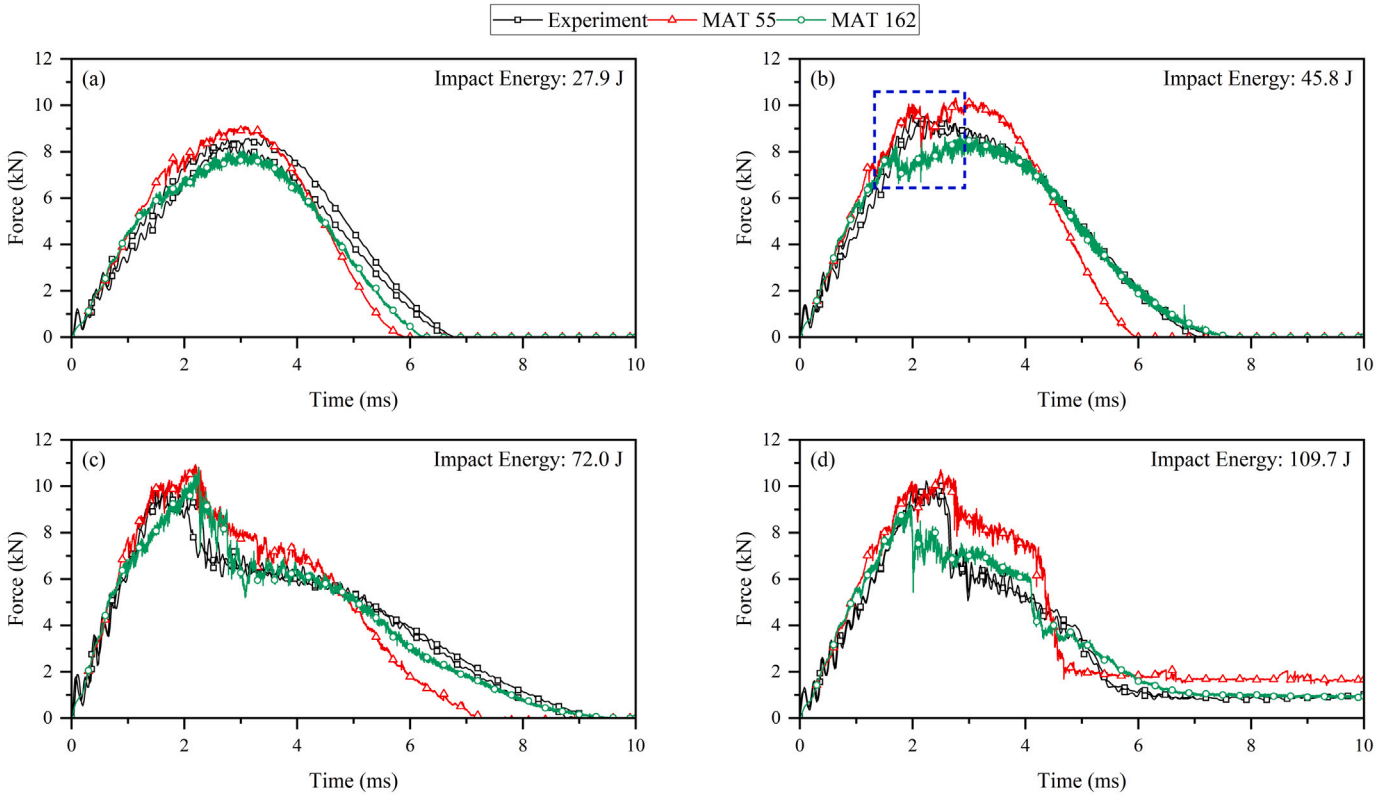

Fig. 3. Comparison of the numerical prediction by MAT 55 and MAT 162 models against the experimental force–time plot for the different impact energies: (a) 27.9 J, (b) 45.8 J, (c) 71.3 J, and (d) 109.7 J.

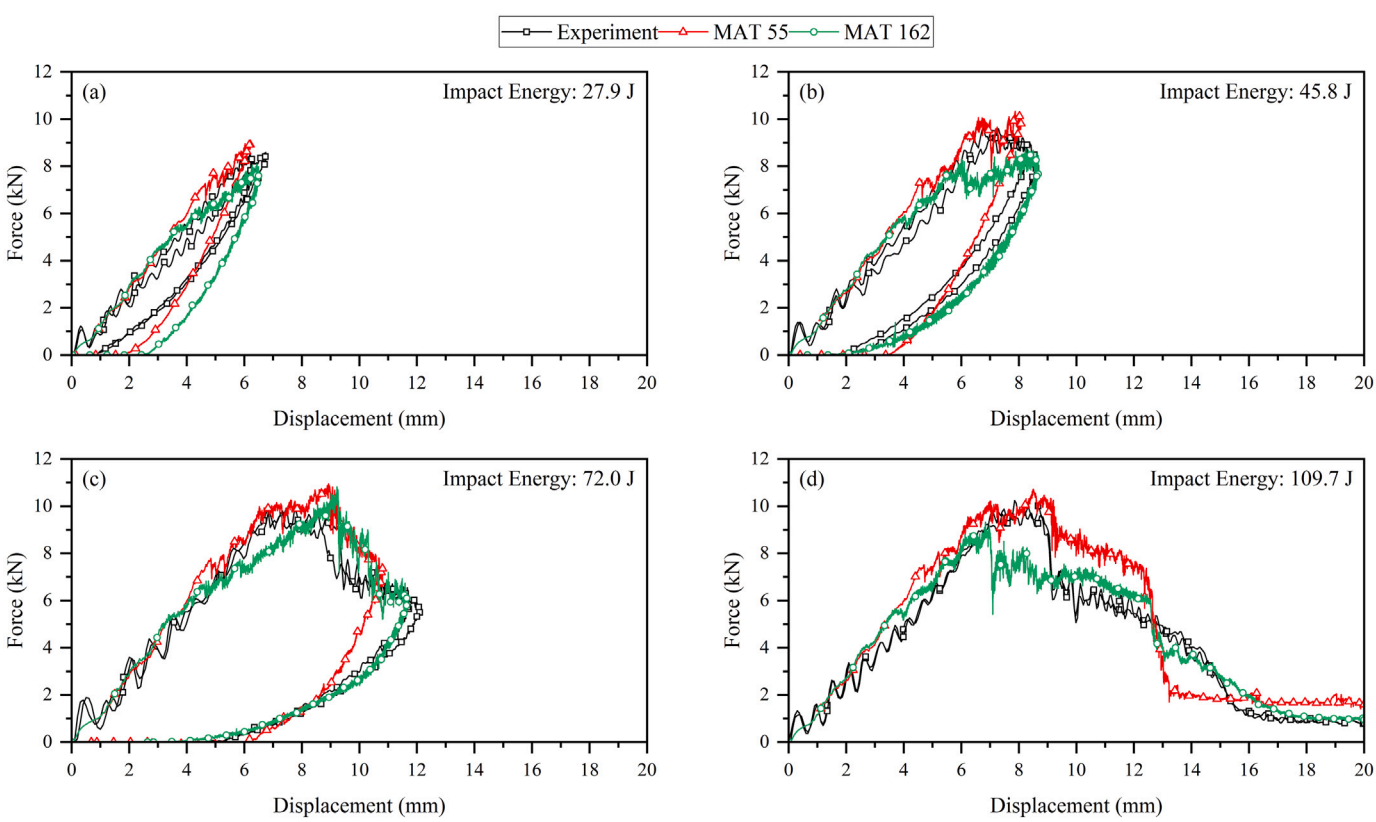

Fig. 4. Comparison of the numerical prediction by MAT 55 and MAT 162 models against the experimental force–displacement plot for the different impact energies: (a) 27.9 J, (b) 45.8 J, (c) 71.3 J, and (d) 109.7 J.

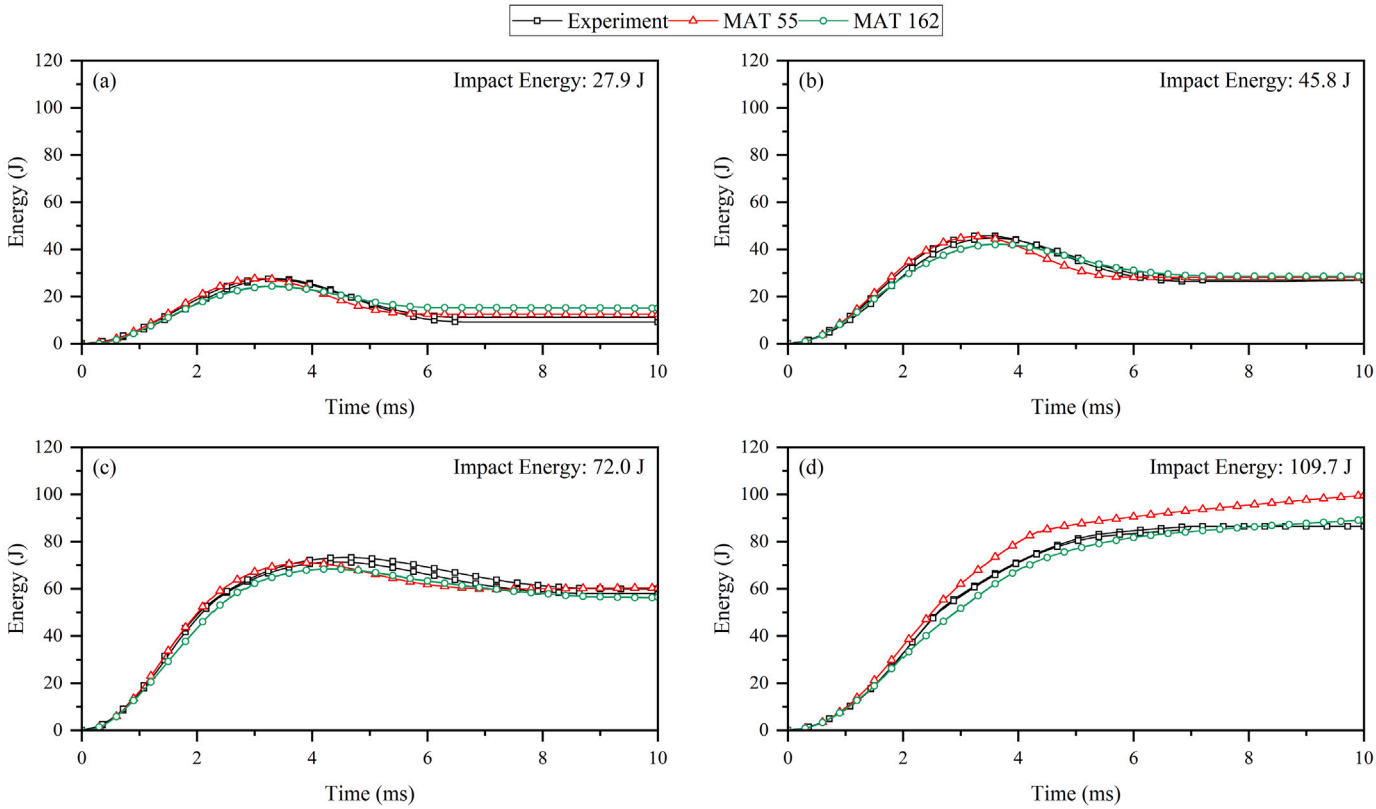

Fig. 5. Comparison of the numerical prediction by MAT 55 and MAT 162 models against the experimental energy–time plot for the different impact energies: (a) 27.9 J, (b) 45.8 J, (c) 71.3 J, and (d) 109.7 J.

Table 5
Experimental and numerical comparison of peak force, peak displacement, and dissipated energy of impacts at different energies.

Impact energy [J]	Peak force [kN]			Peak displacement [mm]			Dissipated energy [J]		
	Exp	MAT 55	MAT 162	Exp	MAT 55	MAT 162	Exp	MAT 55	MAT 162
27.9	8.52	9.10	7.92	6.23	6.21	6.48	11.23	12.50	15.70
Deviation (%)	–	6.81	−7.04	–	−0.32	4.01	–	11.31	39.80
45.8	9.31	10.33	10.34	8.45	8.08	8.26	26.98	28.13	29.70
Deviation (%)	–	10.96	11.06	–	−4.40	−2.25	–	4.26	10.08
72.0	9.89	10.94	8.99	12.00	10.81	12.24	59.85	60.25	60.62
Deviation (%)	–	10.62	−9.10	–	−9.95	2.00	–	0.67	1.29
109.7	10.24	10.72	9.48	–	–	–	86.44	99.30	92.05
Deviation (%)	–	4.69	−7.42	–	–	–	–	14.88	6.49

energies does not employ element erosion. In the same context, the energy dissipation estimation at highest energy (109.7 J) by MAT 55 shows significant error with the experimental results. The results for the peak force, peak displacement, and dissipated energy captured by these simulations at all four energies have been quantified in Table 5 with the deviation obtained with respect to the experimental dataset. The error in peak impact force was lower than 11% for all impact energies, while excellent resemblance in terms of the peak displacement has been captured by the models in all energy cases with the highest deviation of only 4%. Relatively larger errors were obtained in the predictions of dissipated energies, especially in the 27.9 J energy case, which can be attributed to the different energy absorption mechanisms at different impact energy levels, similar observations have been reported in [89,105,106].

The driving damage mechanisms for such woven composites involve fiber breakage, matrix cracking, delamination, and permanent indentations [78,107,108], and they were successfully captured by both the material models considered in this study. Based on the different damage mechanisms, it has been observed that the MAT 55 models was more accurate in predicting the response at the lower energy, as also concluded by previous studies [68,89]. Meanwhile, MAT 162 with the ability to consider the strain-rate effect was able to perform better than MAT 55 at higher energies, due to better prediction of the fiber failure and delamination which caused major drops in the mechanical response and contributed to energy absorption [71]. Fig. 6 shows the penetration of the impactor over the duration of the numerical simulations based on both the material models at the highest energy (109.7 J), respectively. The velocity–time plot for the impactor in both the material model cases has been depicted in Fig. 6c. It can be observed that the impactor penetrated through the laminate sooner and this results in a reduction in the damage propagation within the laminate, whereas the impactor in the case of MAT 162 moves more progressively through laminate, hence demonstrating superior performance in prediction of progressive damage.

5.2. Damage morphology and delamination

The damage morphology obtained in each experimental impact energy case has been compared against the numerical prediction generated by both material models in the preceding section. Emphasis has

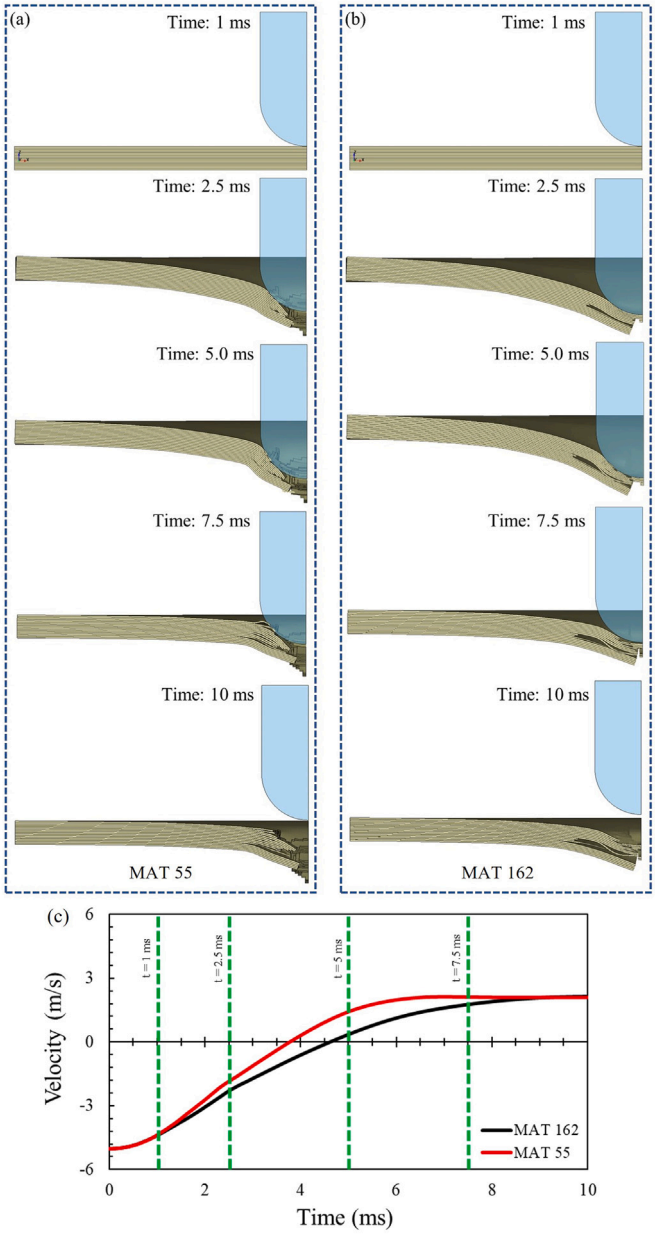

Fig. 6. Comparison of numerical steps of 109.7 J energy rigid impactor penetrating through the laminate based (a) MAT 55 and (b) MAT162 material models. (c) The velocity–time plot traced down to demonstrate the rebound response of the impactor predicted by both numerical models.

been made on the resemblance of the damage patterns in the cross-sectional view as shown in Fig. 7 and the back side of the laminate as shown in Fig. 8. Both models simulate permanent deformation after low-velocity impact by incorporating irreversible interlaminar and intralaminar damage mechanisms, achieved through (i) delamination and frictional interactions that prevent layer reversion, and (ii) intralaminar matrix and fiber damage leading to reduced stiffness or removal of elements, thereby hindering elastic rebound. The cross-sectional damage morphology depicts the dominance of the fiber failure in the lower energy cases (27.9 and 45.8 J) which was successfully accounted by both the material model predictions, shown in Fig. 7. In the case of 45.8 J, the resulting impact bulge due to severe fiber failure correlates with the sudden drop in the peak force value, as marked in the box in Fig. 3b. Also, a larger damaged area and higher energy absorption were experienced as the delamination areas tend to propagate over the higher energy cases (72.0 and 109.7 J). The penetration threshold is the average energy between the highest partial penetration and lowest full perforation energies from the experimental results [103]. For impacts above the threshold, the impactor fully perforated the specimen and did not rebound and this is consistent with the literature [78,109,110].

MAT 55 depicts a wider span and excess element erosion at the center of the laminate due to the directional misguide in the propagation of the failure mode. The permanent deformation and the formation of plastic hinge after impact can be seen in both experimental and numerical images. At the perforation limit energy (109.7 J), the extensive delamination and the deformation of the lamination have been accurately predicted by the numerical models, however, the MAT 55 tends to have excessive element erosion and does not demonstrate the petal formations on the edge of the damage well. This can also be determined from the force–displacement response (Fig. 4d), where the laminate inherits more force with longer displacement during the impact, which results in higher energy absorption during the perforation, as shown in Fig. 5d.

The delamination profile obtained through numerical simulations for all the energy cases is compared with the experimental data in Fig. 9a and the quantification of the damaged area done using the ImageJ software has been summarized in Fig. 9b. The damage pattern evolves nearly uniformly in both the direction of the laminate due to its woven architecture [111]. A significant increase in delamination can be observed in experimental results as well as numerical studies as the impact energy tends to reach the penetration limit. Morphologically, a better estimation of the delamination area has been observed in the numerical simulations based on MAT 162 due to improved definitions for the failure modes. However, the models overpredict the damaged area with an error of −29.0% and −33.5% in the case of 72.0 J and 109.7 J energies. On the other hand, MAT 55 prediction capabilities improve at the higher energies with a maximum error of −16.78%. At the rebounding energies (27.9 J and 45.8 J), the MAT 162 material model demonstrated good results within the error range of 10.7%.

5.3. Parametric study of the non-physical parameters defined in the material models

Upon gaining a fundamental intuition into the competencies of MAT 55 and MAT 162 in simulating the low-velocity impact response of woven fiber composites, the investigations are further expanded to provide further insight into the influence of several numerically calibrated input parameters. This is a fundamental task since the non-physical input parameters (summarized in Table 4) are abundant in both MAT 55 and MAT 162 and the acceptable trend among researchers [54,60,62,74] is the use of the trial-and-error approach to find the suitable input values for the models. Whereas for doing this, a thorough understanding of the sensitivity of the models to the input data is required since a slight change in some of the studied parameters of this section can result in a remarkable change in the prediction capabilities of the FE models. Therefore, in this section, hourglass control value, parameters affecting repressive failure, element deletion, and strain-rate sensitivity have been thoroughly discussed.

5.3.1. Effect of Hourglass control

Hourglass modes refer to modes of deformation that have zero energy, produce no strain or stress, and are therefore non-physical in nature. Since single-integration elements are used for the FE models, to avoid the hourglass modes, both FE models based on MAT 55 and MAT 162, use the hourglass control option. There are several hourglass control options such as standard, Flanangan–Belytschko and Belytschko–Binderman available in LS-Dyna [112] and it has been shown that the input for the hourglass control has a significant effect on the response of the low-velocity impact models. The most concerning output when checking for the correctness of the hourglass control inputs is the hourglass energy dissipation in the model. The rule of thumb

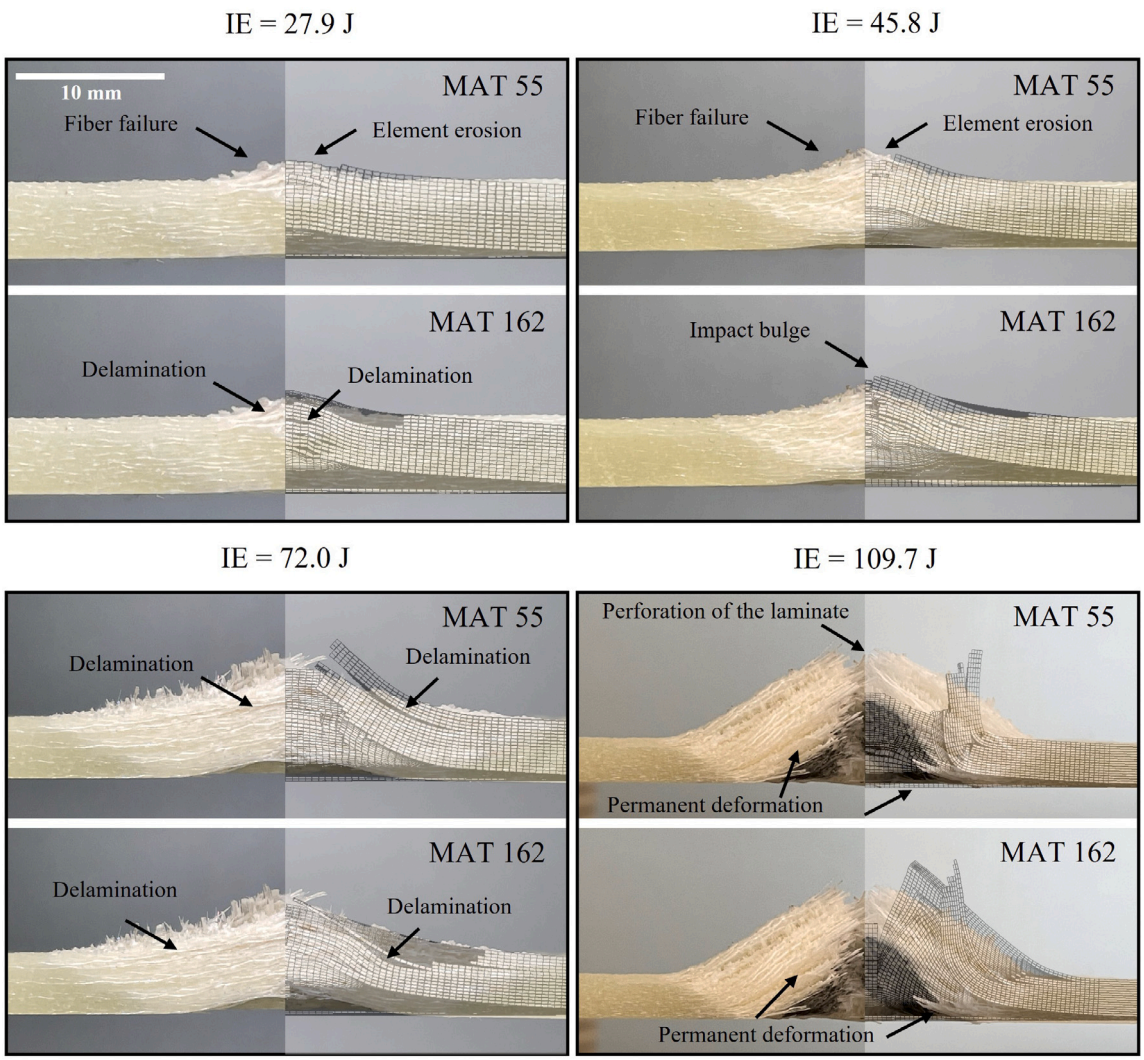

Fig. 7. Comparison of the experimentally-and numerically-predicted damage morphology at the cross-section of the laminate by MAT 55 and MAT 162 material models for all the impact energies ranging from 27.9 J to 109.7 J. In each of the sub-figures, the arrows show the type of failure occurring in between the plies of the laminate, namely fiber failure, delamination, and permanent deformation.

is that the hourglass energy should be less than 10% of the model's internal energy during the simulation [87]. Stiffness-based hourglass control has been suggested for simulations of low-velocity impact, thus, here, type 5 of hourglass control, i.e., Flanagan–Belytschko stiffness form with $QM = 0.2$ had been used [86,88,113]. Figs. 10a and b show the effect of the hourglass control coefficient on the hourglass energy dissipation and force–displacement response for the 72.0 J impact. It can be observed from Fig. 10a that the hourglass energy is below the 10% threshold for models with type 5 hourglass control regardless of the *QM* coefficient value while Fig. 10b shows that changing the hourglass coefficient significantly changes the low-velocity impact response prediction as also reported in [69]. As expected, higher hourglass values led to a stiffer behavior [114], and a better correlation with the experimental data was observed for the model with a *QM* value of 0.25 as indicated by better prediction of the impact bending stiffness in Fig. 10(b). The hourglass energy control parameters are required to avoid numerical instabilities, especially in terms of the contact stiffness between indenter and the laminate, as amount of non-physical energy is contributed through deformation experienced by elements in the model. The coefficient of hourglass energy alters the overall bending stiffness as it is evidently to be the predominant reaction for the laminate under impact loading [69,87]. The contact force experienced by the indenter increases proportionally with the coefficient of hourglass energy in case of stiffness-based hourglass control.

5.3.2. Parameters affecting the progressive failure

In this section, a parametric study has been performed on the non-physical input parameters governing the post-damage behavior of the material models (MAT 55 and MAT 162) used in this study. MAT 55 does not inherently include a progressive failure model and considers the post-impact behavior using minimum stress limit parameters *(SLIMT)* corresponding to different failure modes. In contrast, MAT 162 incorporates progressive failure modeling capabilities by using non-linear softening parameters (*AM1-4*, see Eq. (A.28) in Appendix A) [115] making it more suitable for cases where materials undergo complex failure processes. Figs. 11 and 12 show the sensitivity of the low-velocity impact response to the progressive failure parameters in the case of MAT 55 and MAT 162, respectively. In Fig. 11, *SLIMT1* (minimum stress limit factor for fiber tension failure) values of 0.0001, 0.5, and 1 were considered and it was observed that the impact response is highly sensitive to changes in the *SLIMT* parameter. The damage contour in Fig. 11 shows that lower values of *SLIMT* not only led to an overestimation of the damaged area and initiation of the damage outside of the contact zone but also led to the change of impact response from rebounding to perforation [103] for *SLIMT* values of 0.0001 and 0.5. Comparing different *SLIMT* values, it is noted that higher *SLIMT* values exhibit a stronger correlation with experimental results with a 39.5%, −12.5%, and −9.9% error in

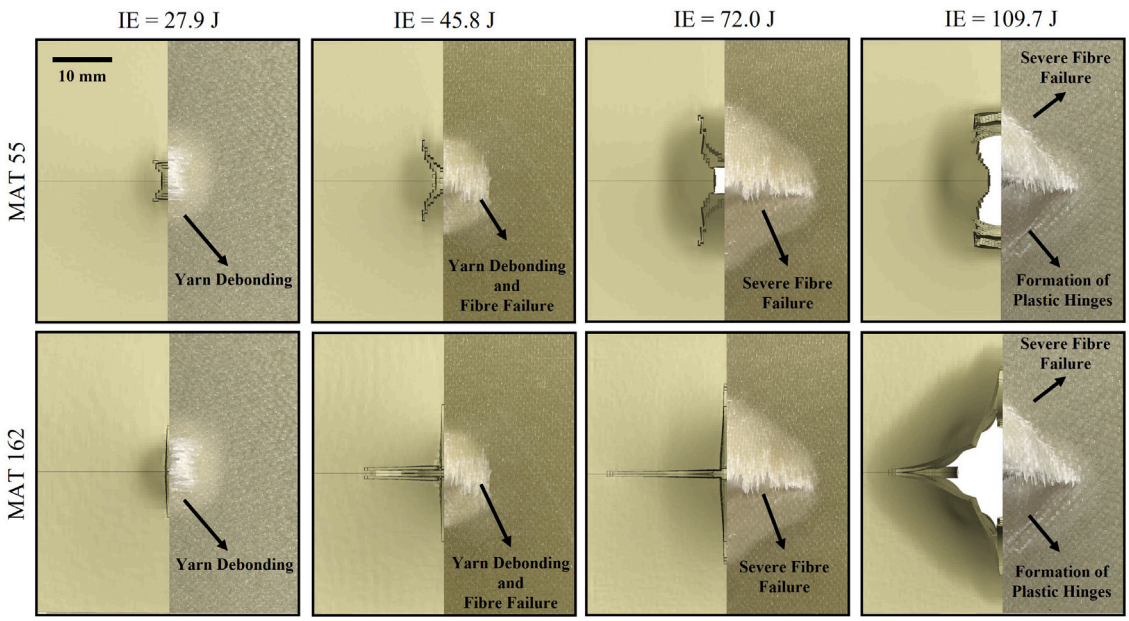

Fig. 8. Comparison of the experimentally- and numerically-predicted damage morphology on the back side of the laminate by MAT 55 and MAT 162 material models for all the impact energies ranging from 27.9 J to 109.7 J. In each of the sub-figures, the arrows show the type of failure occurring in between the plies of the laminate, namely fiber failure, delamination, yarn debonding, and formation of plastic hinge.

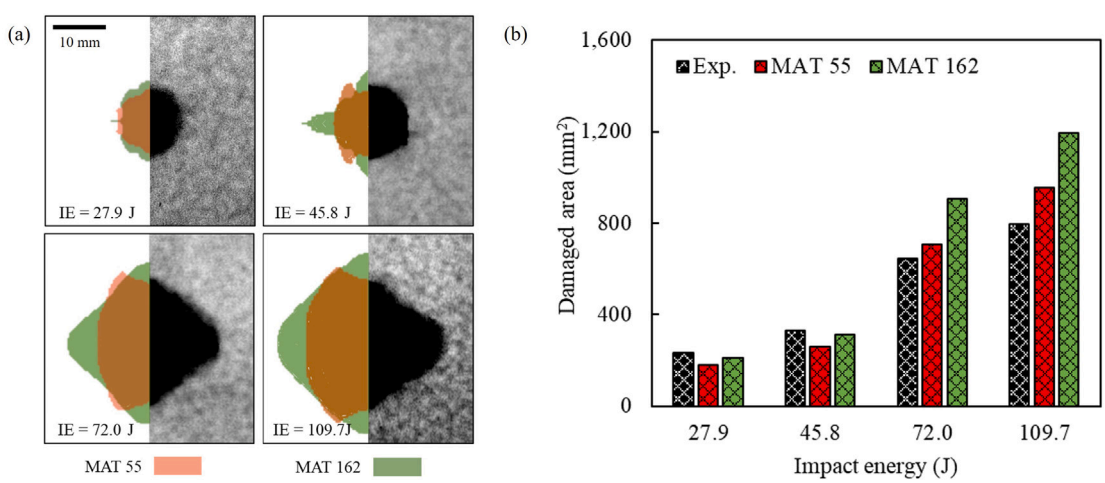

Fig. 9. (a) Estimation of delamination area obtained through both numerical models against the ImageJ processed experimental results, and (b) quantitative comparison of the damage areas prediction by the numerical models and experiments for all the four impact energies considered in this study.

prediction of maximum force for simulation with *SLIMT1* of 0.0001, 0.5, and 1, respectively.

Another parameter affecting the progressive failure in MAT 55 is the *SOFT* or crush front reduction factor (see Appendix A), and Fig. 12 explores the sensitivity analysis of this non-physical input parameter within the acceptable range of [0, 1] in the MAT 55 material model. *SOFT* values close to zero indicate near complete strength reduction at the crush front, while values close to one represent no strength reduction. The main purpose of the crush front reduction factor is to prevent instability and ensure stable failure as the impact load is transitioned from the active row of elements to the next row [54,116]. Likewise, the results of Fig. 12 highlight the significant influence of the *SOFT* parameter on the predicted low-velocity impact response, and as expected lower values of *SOFT* led to a reduction in load-bearing capacity and higher deformation. Extremely low values of the *SOFT* parameter (the green curve in Fig. 12) lead to a perforation response which did not correlate well with the rebounding response observed from the experiment. The models with *SOFT* parameter values of 0.35, 0.50, and 0.75 predicted the experimental peak force with a deviation of −8.7%, −17.2%, and −22.5%, respectively. Also, better agreement in the prediction of impact bending stiffness and deformation of the laminate was observed for the model with a *SOFT* value equal to 0.35, thus this *SOFT* value was chosen for subsequent simulations.

Figs. 13a and b show the sensitivity of the LVI model to the input parameters related to the progressive failure in MAT 162, i.e., the fiber failure modes softening coefficients (*AM1 and AM2* — Fig. 13a) and matrix failure mode softening coefficients (*AM4* — Fig. 13b) in the fabric lamina model [112]. It can be observed that increasing these softening parameters leads to lower impact bending stiffness and peak force and higher deformation in the laminate which is consistent with previous studies in [73,117]. A fiber failure mode softening coefficient close to zero led to better agreement with the experimental results and correlated well with the simulations with MAT 55 (Fig. 11). It was observed that in both material models, insubstantial degradation after damage initiation would lead to better simulation results. In addition, higher values of fiber failure modes softening coefficients

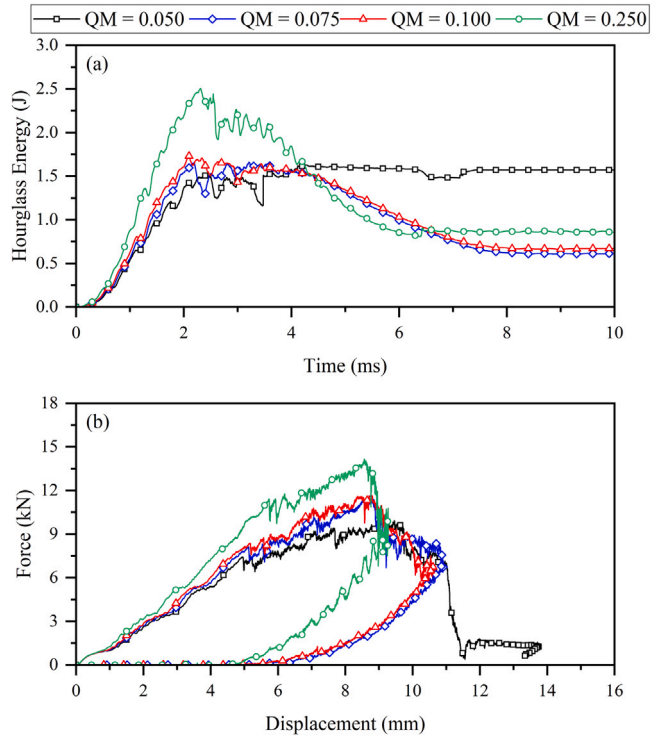

Fig. 10. Comparison of hourglass coefficient effect for a low-velocity impact simulation with 72.0 J energy, (a): Hourglass energy, and (b): Force–displacement curves.

changed the low-velocity response from rebounding to perforation and proved not suitable for simulations of this study. Fig. 13b shows the lower sensitivity of the model to the matrix failure softening coefficient resulting in a fairly acceptable curve regardless of the input values used for the *AM4*. The calibration procedure performed in this subsection corresponds to the need of adequately tune the developed numerical models for capturing correct dominating failure modes in the laminate. It has also been observed that under the low-velocity impact, the fiber contributes more resisting the impacted load [118,119].

5.3.3. Effect of element erosion

The sensitivity analysis for the element erosion criterion is shown in Figs. 14 and 15 for MAT 55 and MAT 162, respectively. In both of these material models, a strain-based criterion is available for element erosion. Element erosion criterion is a non-physical input parameter and is normally calibrated by following a trial-and-error basis due to its dependency on mesh size, element type, and material model inputs [32,120]. It has been shown that element erosion highly impacts the simulation results of composites that undergo failure [121,122]. The influence of effective failure strain *(EFS)* on the force–displacement response obtained from a simulation with MAT 55 is shown in Fig. 14. The higher effective failure strain values corresponded to increased peak force and bending stiffness, indicating enhanced resistance to deformation and greater load bearing capacity. Conversely, lower effective failure strain values resulted in perforation or failure at lower forces, indicating an underprediction of the laminate's load-bearing capacity. The model predicted the impact peak force with a deviation of 66.2%, −12.9%, −31.0% and −37.4% for the effective failure strain values of 0.10, 0.28, 0.40, and 0.55, respectively, indicating a better agreement with the experimental observations for an input value of 0.28. The damaged contours in Fig. 14 show that in the models with lower values of *EFS (EFS = 0.1 and EFS = 0.28)*, the removed elements are limited to the rear side of the laminate which experiences higher values of bending stress and more deformation. Meanwhile, for the model in agreement with the experiment *(EFS = 0.4)*, element removal of the impact side was also observed.

Similarly, the effect of failure strain (*ELIMIT*: normal in-plane strain) on the simulation result with MAT 162 is shown in Fig. 15. The force–displacement responses of Fig. 15a for different values of *ELIMIT* showed lower sensitivity to the input values compared to the similar simulation results of MAT 55 in Fig. 14. Likewise, low values of *ELIMIT* led to a response closer to perforation which was not in agreement with experimental observations. Fig. 15b shows the corresponding contour plots of the damaged area of the curves in Fig. 15a, where more dispersed and complex patterns of element removal can be observed compared to MAT 55. This can be attributed to the lack of presence of a crash front algorithm and a more complex definition of multi-mode failure in MAT 162.

5.3.4. Effect of strain-rate sensitivity

The effect of strain rate sensitivity on the simulation results of low-velocity impact has been demonstrated in Fig. 16. When selecting a material model for simulating low-velocity impact in composites, it is crucial to consider the specific behavior of the material and the loading conditions. In the case of low-velocity impact, some works in the literature discarded the effect of strain-rate sensitivity on the simulation result due to the low rate of loading during an impact event [103,123], meanwhile, the simulation results of this work showed a considerable effect by doing a comparative study on models with and without rate sensitivity formulations.

It is important to consider that MAT 55 does not directly account for the strain rate effects on the material's behavior while MAT 162 is specifically designed to incorporate rate sensitivity following Eq. (A.29) (see Appendix A for more details).

$$\{S_{RT}\} = \{S_0\}\left[1 + C_{\text{rate1}}\ \ln\left(\frac{\{\dot{\varepsilon}\}}{\dot{\varepsilon}_0}\right)\right] \tag{1}$$

where C_{rate1} is the strain-rate input constant and S_{RT} are all the strain-rate dependent strength properties. Fig. 16a shows the strain-rate dependent experimental data from [124,125] on E-glass/epoxy composite that has been used to fit the curve of Eq. (1). C_{rate1} defines the strain-rate dependent property for the different strengths of the material system using Eq. (A.29). The model can incorporate this effect using only a single value, hence an average value for the coefficient of strain-rate parameter is considered in this study, as it is commonly done in literature [71,79]. The authors consider this as a homogeneous simplification based on the architecture of the woven composite. The initial value for C_{rate1} (~0.16) was found by averaging the values found in Fig. 16a for different material directions. Using the initial value, a sensitivity analysis was performed to study the effect of strain rate, as shown in the force–displacement curves of Fig. 16b. The results showed that MAT 162 could capture strain rate effects and provide a more accurate representation of the impact response by using a C_{rate1} value of 0.045, corresponding strain rate between 50 to 90 s^{-1}. Higher values of C_{rate1} lead to a stiffer impact behavior compared to the experiment while a C_{rate1} value of zero led to a perforation response. In addition, the comparison of absorbed energy to impact energy for models with and without rate-sensitivity in Fig. 16c (with a reported deviation of −0.35% and −12.9%, respectively) showed significant improvement by using the rate-sensitive model. The damage contours for fiber failure modes in 11 and 22 directions and matrix failure modes of the modes of Fig. 16b are shown in Fig. 16d. Incorporating strain rate sensitivity in the simulation of low-velocity impact had a significant impact on the damage shape and element deletion patterns. When rate sensitivity is not considered (as seen by the first row of contours in Fig. 16d for the model without rate sensitivity) the damage does not tend to concentrate primarily within the contact region leading to a premature perforation response. Fig. 16d shows that by accounting for strain rate sensitivity in the simulation, a more realistic representation of the material's behavior can be achieved.

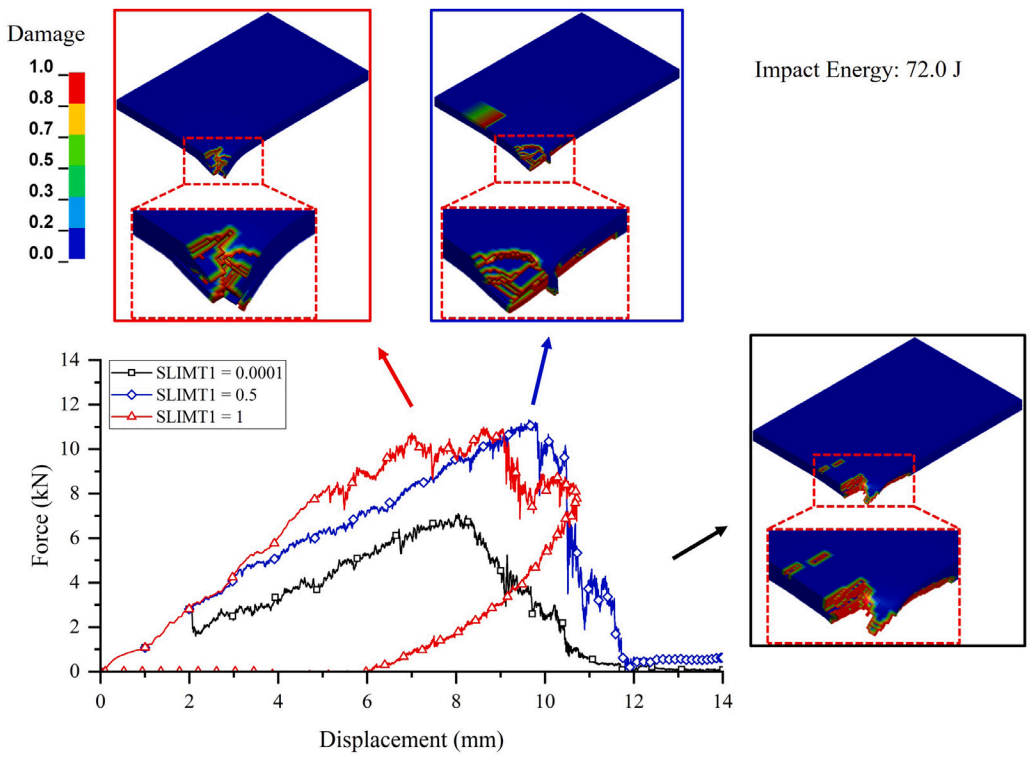

Fig. 11. Force–displacement curves for different *SLIMT1* values in a low-velocity impact simulation using MAT 55.

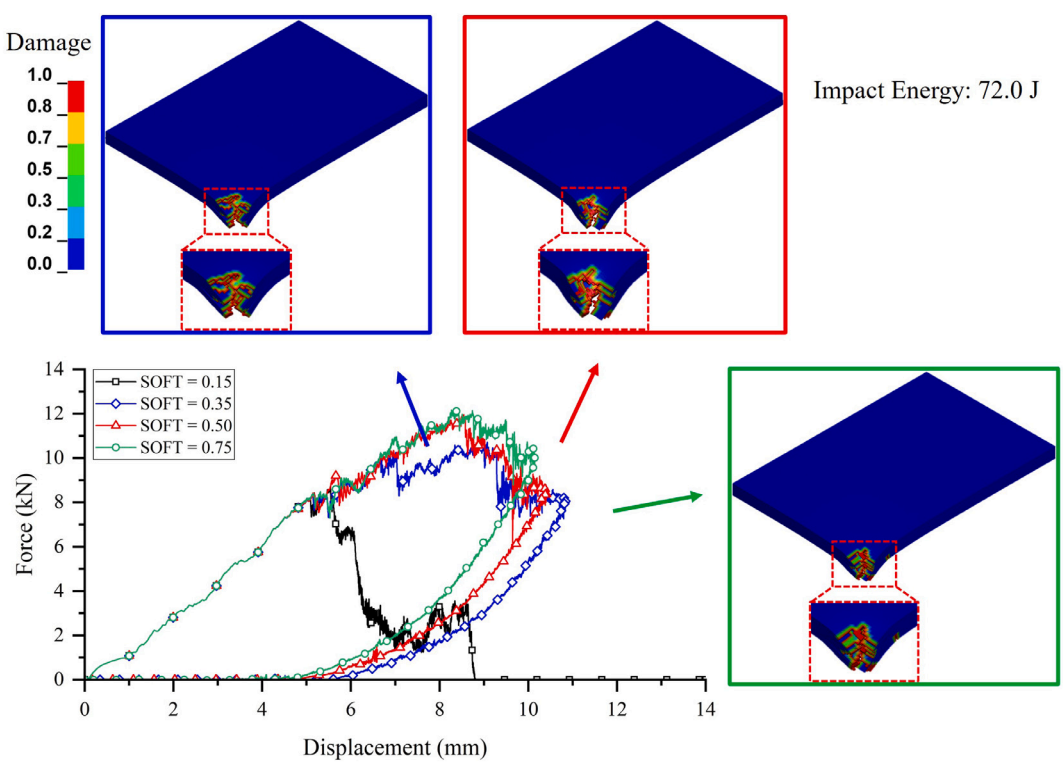

Fig. 12. Influence of *SOFT* parameter variation on the low-velocity impact simulation results using MAT 55.

The developed and calibrated models are compared with existing models from the literature to assess the applicability of the models for the wider spectrum of impact energies, as summarized in Table 6. The models are examined based on the impact energy range considered or exercised, whether the model considers strain-rate effect in the damage laws, and the numerical accuracy achieved. The numerical accuracy has been determined based on the error in the prediction of the peak force obtained numerically and experimentally, shown in the articles. From Table 6, the MAT 162 model presented in this study is capable of predicting the mechanical response of the composite laminate for

Table 6
Comparison of the prediction capability and robustness of the developed models with the existing models from the literature [42,68,89,97,117,126–128].

Author (Year)	Material description	Impact energy range (J)	Material model (Solver)	Strain-rate effect	Numerical accuracy (%)
Present Study	Woven Composite (S2-Glass)	27.9–109.7	MAT 162 (LS-Dyna)	Yes	7.04
Present Study	Woven Composite (S2-Glass)	27.9–109.7	MAT 55 (LS-Dyna)	No	10.96
Xu et al. (2023)	Woven Composite (Glass/Kevlar)	108	MAT 59 (LS-Dyna)	No	15.23
Ge et al. (2022)	Woven Composite (T300-3 K)	16–283	VUMAT (ABAQUS)	No	10.67
Albayrak et al. (2022)	Glass Fiber/Epoxy Composite	40	MAT 162 (LS-Dyna)	Yes	4.20
Ma et al. (2021)	Woven Composite (Kevlar)	30–45	MAT 162 (LS-Dyna)	Yes	7.47
Cheng et al.(2020)	Woven Composite (3238A/CF3052)	22–50	Hashin Criteria (ABAQUS)	No	13.50
Sy et al. (2019)	Carbon/Epoxy UD Composite (FlaxPly UD150)	5–30	MAT 55 (LS-Dyna)	No	26.00
Miao et al. (2019)	Woven Composite (T700SC-12 K)	30	VUMAT (ABAQUS)	Yes	3.60
Berk et al. (2015)	Aramid/epoxy Composite	20–30	MAT 55 (LS-Dyna)	No	18.30

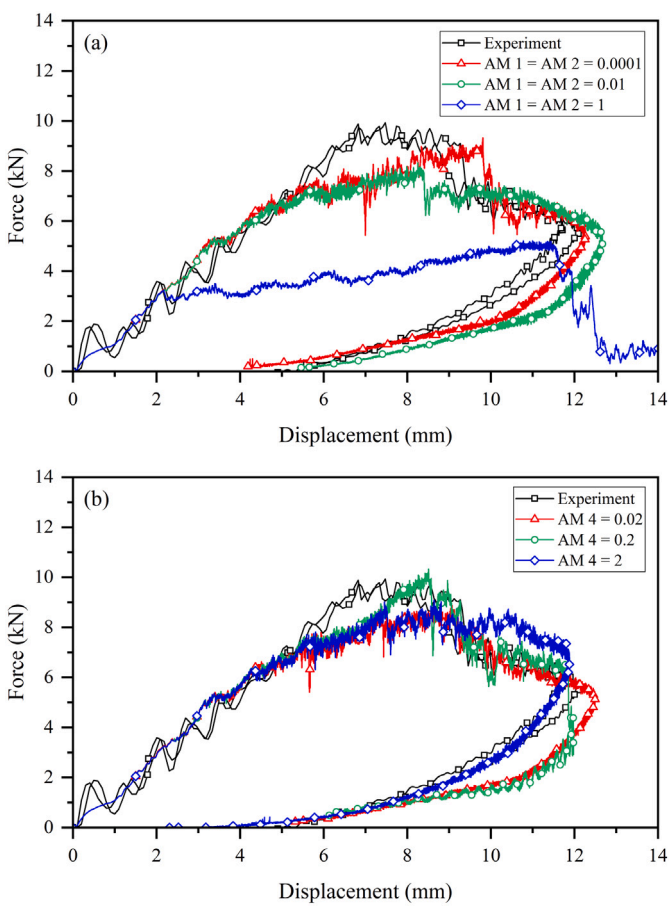

Fig. 13. Effect of progressive damage parameters variation on the force–displacement curve for a 72.0 J low-velocity impact simulation using MAT 162, (a): Fiber failure modes softening coefficients, and (b): Matrix failure softening coefficient.

a wider range of impact energies with good benchmark performance. On the other hand, MAT 55 in the present study is reasonable good in prediction capability but lacks the consideration of strain-rate effect, which has a substantial contribution to the mechanical response of the laminate for relatively higher impact energies.

6. Conclusion

In this work, a comprehensive study has been conducted on the low-velocity performance of woven composites based on two progressive damage models (MAT 55 and MAT 162) from the LS-Dyna directory. We first demonstrated the prediction capabilities of both finite element models by comparing the mechanical response of S2 glass woven laminates under low-velocity impact for four energy cases against the experimental data. Secondly, the damage morphology and delamination propagating with increasing impact energy were discussed in details, with an emphasis on the dominating failure modes occurring in the laminate at different energies. Then, a parametric study on the non-physical parameters present in both of these material models were conducted. The major conclusions from this study are as follows:

1. Overall, MAT 55 models were more accurate for lower impact energies, while MAT 162 models performed better for higher impact energies, attributed to their consideration of strain-rate effects. Both models shows satisfactory agreement with experimental data for different energy levels and failure modes.
2. The results highlight the significant contribution of fibers in bearing the low-velocity impact load during the impact event as indicated by high sensitivity of the simulation results to the fiber strain-softening parameter. Meanwhile, the model did not show such sensitivity to matrix stain-softening parameter.
3. Lower effective failure strain *(EFS)* values result in MAT 55 depicts the early failure of the laminate, indicating an under-prediction of the laminate's load-bearing capacity. However, more dispersed and complex patterns of element removal was observed in MAT 162, which can be related to the more complex definition of multi-mode failure.
4. A significant effect on the impact response, element deletion, and damage morphology were observed when considering the strain-rate effect for the low-velocity impact models using MAT 162. By neglecting the strain-rate sensitivity (C_{rate1} = 0), premature perforation response occurred which was not consistent with the experimental observations.

Due to the more straightforward characterization of failure modes and the presence of the non-linear behavior, superior predictions by MAT 55 models at lower energy demonstrated that this material model may be better for forecasting the structural response of composite structures. However, the more delicate definition of failure criteria in MAT 162 showed superior results in predicting catastrophic failure and perforation. This was due to the better definition of progressive damage and inclusion of strain-rate sensitivity, which significantly affected the low-velocity impact response of the laminate. This work provides insights into the calibration of the material models, optimization, and influence of the various non-physical entities involved in the FEM model, including the effect of incorporating strain-rate dependency in the model.

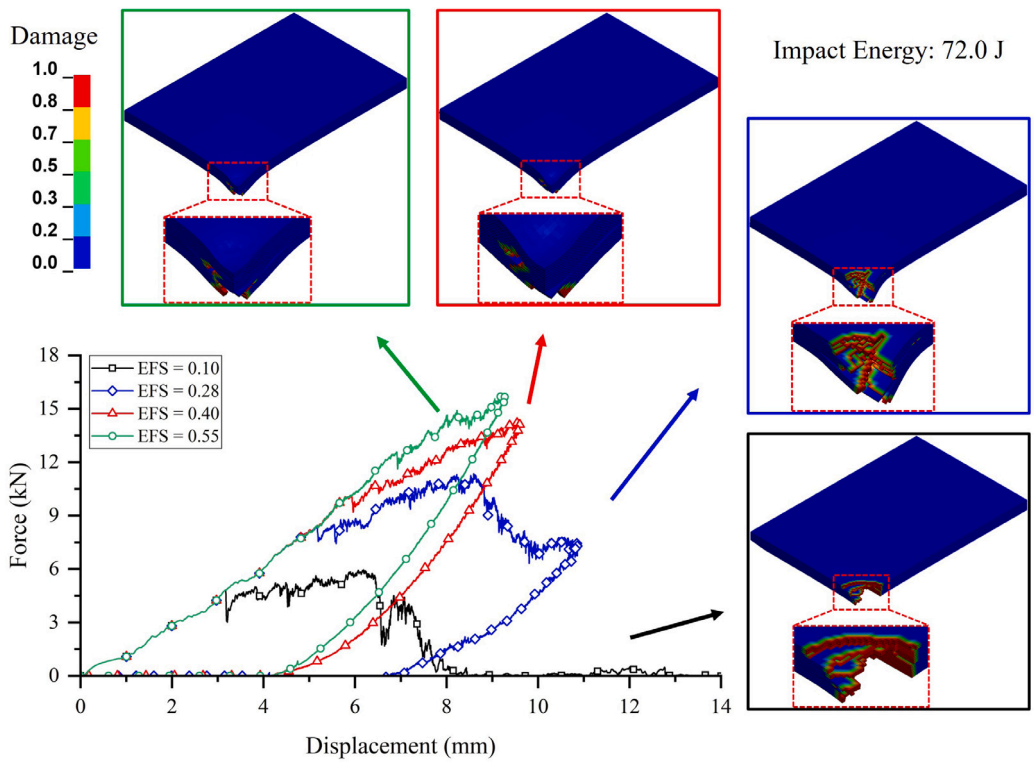

Fig. 14. Influence of effective failure strain values for element erosion on the force–displacement response of the laminate subjected to 72.0 J impact modeled with MAT 55.

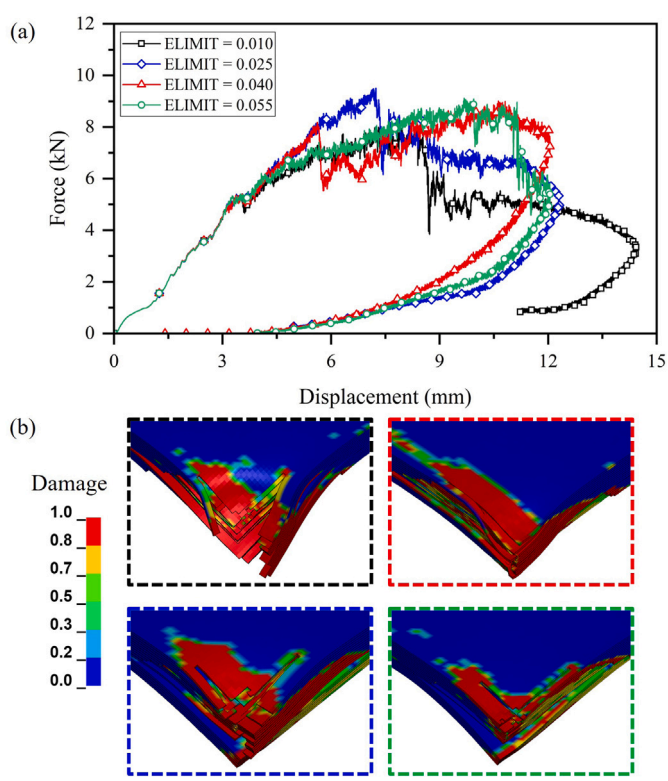

Fig. 15. Influence of failure strain values for element erosion on the response of the laminate subjected to 72.0 J impact modeled with MAT 162, (a): Force–displacement curves, and (b): Resulted damage in the contact region.

CRediT authorship contribution statement

Yogesh Kumar: Writing – original draft, Visualization, Validation, Software, Methodology, Investigation, Formal analysis, Conceptualization. **Mohammad Rezasefat:** Writing – original draft, Validation, Methodology, Conceptualization. **Sandro C. Amico:** Writing – review & editing, Resources. **Andrea Manes:** Writing – review & editing, Resources. **Patricia I. Dolez:** Writing – review & editing, Supervision. **James D. Hogan:** Writing – review & editing, Supervision, Resources, Conceptualization.

Declaration of competing interest

The authors declare that they have no known competing financial interests or personal relationships that could have appeared to influence the work reported in this paper.

Data availability

Data will be made available on request.

Acknowledgments

This work is supported by Defence Research and Development Canada (DRDC), General Dynamics Land Systems – Canada, and NP Aerospace through NSERC Alliance project ALLRP 560447-2020. The views and conclusions contained in this document are those of the authors and should not be interpreted as representing the official policies, either expressed or implied, of General Dynamics, NP Aerospace, DRDC or the Government of Canada. The Government of Canada is authorized to reproduce and distribute reprints for Government purposes notwithstanding any copyright notation herein.

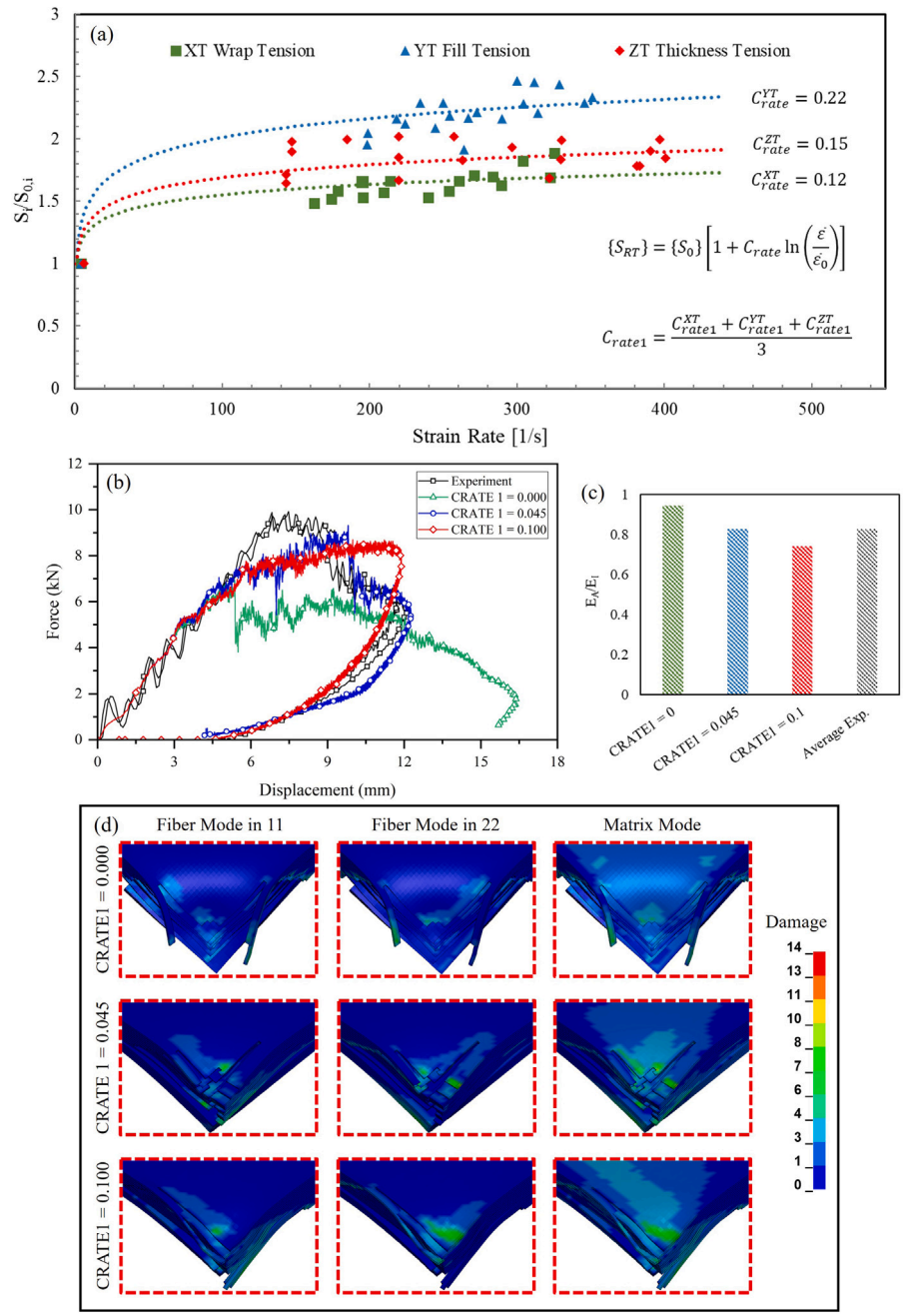

Fig. 16. Sensitivity analysis on the effect of strain-rate sensitivity on the low-velocity impact response, (a): Strain-rate dependent strength in different directions (XT = tensile strength in wrap direction, YT = tensile strength in fill direction and ZT = tensile strength in through-thickness direction) taken from experimental data of [124,125], (b): Force–displacement curves for models with and without strain-rate sensitivity, (d): Effect of strain-rate sensitivity on the prediction of absorbed energy, and (d): contour plots of fiber and matrix mode damage for models with and without strain-rate sensitivity.

Appendix A. Constitutive model description

A.1. MAT 55 enhanced composite damage model

With the MAT 55 material card, the modes of the tensile and compressive fiber are driven as in the Chang-Chang criteria [90], and the tensile and compressive matrix failure are defined by the Tsai–Wu criteria [91]. The failure modes are formulated accordingly:

For the tensile fiber mode:

$$\sigma_{aa} > 0 \Rightarrow e_f^2 = \left(\frac{\sigma_{aa}}{X_t}\right)^2 + \beta\left(\frac{\sigma_{ab}}{S_c}\right)^2 - 1 \tag{A.1}$$

$$e_f^2 \geq 0 \Rightarrow failed \tag{A.2}$$

$$e_f^2 < 0 \Rightarrow elastic \tag{A.3}$$

$$E_a = E_b = G_{ab} = \nu_{ba} = \nu_{ab} = 0 \tag{A.4}$$

For the compressive fiber mode:

$$\sigma_{aa} < 0 \Rightarrow e_c^2 = \left(\frac{\sigma_{aa}}{X_c}\right)^2 - 1 \tag{A.5}$$

$$e_c^2 \geq 0 \Rightarrow failed \tag{A.6}$$

$$e_c^2 < 0 \Rightarrow elastic \tag{A.7}$$

$$E_a = \nu_{ba} = \nu_{ab} = 0 \tag{A.8}$$

For the tensile and compressive matrix mode:

$$e_{md}^2 = \frac{\sigma_{bb}^2}{Y_c Y_t} + \left(\frac{\sigma_{ab}}{S_c}\right)^2 + \frac{(Y_c - Y_t)\sigma_{bb}}{Y_c Y_t} - 1 \tag{A.9}$$

$$e_{md}^2 \geq 0 \Rightarrow failed \tag{A.10}$$

$$e_{md}^2 < 0 \Rightarrow elastic \tag{A.11}$$

The post-damage behavior and material degradation follow the definition of the *SOFT* parameters. When one of the failure modes is initiated from the Chang-Chang failure criteria, the strength reduction factors, or damage factors get involved with the material strength properties when the matrix starts to crack. Fiber tensile strength softening factor *(FBRT)* and fiber compressive strength softening factors *(YCFAC)* are described by the following equations:

$$X_{t'} = X_t \times FBRT \tag{A.12}$$

$$X_{c'} = Y_c \times YCFAC \tag{A.13}$$

When the stresses in each ply approach the failure strain thresholds, the elements may also be deleted. The maximal tensorial shear strain and the tensile failure strain in the fiber direction are known as *DFAILS* and *DFAILT* in the case of unidirectional tape. Whereas *DFAILC* and *DFAILM* are the compressive failure strain in fiber direction and maximum strain for tensile or compressive matrix straining, respectively. In this investigation, the equations that result from dividing the strength by the corresponding modulus were used to determine the strain values as reported by [112,129], as summarized below:

$$DFAILT = \frac{X_t}{E_a} \tag{A.14}$$

$$DFAILC = \frac{X_c}{E_a} \tag{A.15}$$

$$DFAILM = \frac{Y_t, Y_c}{E_b} \tag{A.16}$$

$$DFAILS = \frac{S_c}{G_{ab}} \tag{A.17}$$

After the current row of components is removed, the crash front reduction factor *(SOFT)* in the material definition lowers the strength of the parts in the subsequent row [55]. Since this is a non-physical cost-effective interpretation of the material's damage zone, the SOFT parameter spans from 0 to 1, with 0 representing no strength drop in the model prior to failure.

A.2. MAT 162 composite MSC damage model

This progressive damage model is governed by Hashin failure criteria [94] and post-damage softening suggested by Matzenmiller et al. [95]. The detailed formulation can be found in [112,130]. *AMODEL* provides an option to define the model for a unidirectional layer or for a fabric layer composite. In the fabric model, the element can be removed if it exceeds the fiber tensile failure in both in-plane directions predicted in the element and the axial tensile strain is greater than defined *ELIMIT*. Following are the concerned equation used by the material model for the fabric lamina [94,95,112]:

For the fiber failure criteria in fill and warp directions:

$$f_6 = \left(\frac{\langle \sigma_a \rangle}{S_{aT}}\right)^2 + \frac{(\tau_{ab}^2 + \tau_{ca}^2)}{S_{aFS}^2} - 1 = 0 \tag{A.18}$$

$$f_7 = \left(\frac{\langle \sigma_b \rangle}{S_{bT}}\right)^2 + \frac{(\tau_{ab}^2 + \tau_{bc}^2)}{S_{bFS}^2} - 1 = 0 \tag{A.19}$$

For the in-plane compressive failure criteria in fill and warp direction:

$$f_8 = \left[\frac{\langle \sigma_a' \rangle}{S_{aC}}\right]^2 - 1 = 0 \tag{A.20}$$

$$f_9 = \left[\frac{\langle \sigma_b' \rangle}{S_{bC}}\right]^2 - 1 = 0 \tag{A.21}$$

$$\sigma_a' = -\sigma_a + \langle -\sigma_c \rangle \tag{A.22}$$

$$\sigma_b' = -\sigma_b + \langle -\sigma_c \rangle \tag{A.23}$$

For the crush failure under compressive pressure:

$$f_{10} = \left(\frac{\langle p \rangle}{S_{FC}}\right)^2 - 1 = 0 \tag{A.24}$$

$$p = -\frac{\sigma_a + \sigma_b + \sigma_c}{3} \tag{A.25}$$

For the in-plane matrix failure mode:

$$f_{11} = \left(\frac{\tau_{ab}}{S_{ab}}\right)^2 - 1 = 0 \tag{A.26}$$

For the through the thickness matrix failure mode:

$$f_{12} = S_{delam}^2 \left\{ \left(\frac{\langle \sigma_c \rangle}{S_{cT}}\right)^2 + \left(\frac{\tau_{bc}}{S_{bc}}\right)^2 + \left(\frac{\tau_{ca}}{S_{ca}}\right)^2 \right\} - 1 = 0 \tag{A.27}$$

Compliance matrix that correlates the damage model proposed by Matzenmiller [95]:

$$\left[C\right] = \begin{bmatrix} \frac{1}{(1-\varpi_1)E_a} & \frac{-\nu_{ba}}{E_b} & \frac{-\nu_{ca}}{E_c} & 0 & 0 & 0 \\ \frac{-\nu_{ab}}{E_a} & \frac{1}{(1-\varpi_2)E_b} & \frac{-\nu_{cb}}{E_c} & 0 & 0 & 0 \\ \frac{-\nu_{ac}}{E_a} & \frac{-\nu_{bc}}{E_b} & \frac{1}{(1-\varpi_3)E_c} & 0 & 0 & 0 \\ 0 & 0 & 0 & \frac{1}{(1-\varpi_4)G_{ab}} & 0 & 0 \\ 0 & 0 & 0 & & \frac{1}{(1-\varpi_5)G_{bc}} & 0 \\ 0 & 0 & 0 & 0 & 0 & \frac{1}{(1-\varpi_6)G_{ca}} \end{bmatrix}$$

$$\varpi_i = 1 - exp\left(\frac{1}{m_j}(1 - r_j^{mj})\right) \tag{A.28}$$

where m_j is the *AM(s)* in the MAT 162 material model description. The four softening parameters control the failure modes in corresponding directions [71]. The Mohr–Coulomb friction parameter *(PHIC)*, which may be measured using an off-axis off-plane compression test technique, is used to account for the impact of compressive stress on shear strengths [131]. The values for the *PHIC* = 10° and *SDELM* = 1.2 were taken from [73] in this study.

The strain-rate sensitivity in the mechanical response of the woven composites is incorporated in the form of a logarithmic function [71,79,112]:

$$\frac{X_{RT}}{X_0} = 1 + C_{rate} \ln\left(\frac{\dot{\bar{\varepsilon}}}{\dot{\bar{\varepsilon}}_0}\right) \tag{A.29}$$

where X_0 is the quasi-static reference property and the X_{RT} is the strain-rate dependent property to be considered at the average strain rate informed using the $\dot{\bar{\varepsilon}}$ term.

A.3. Contact definition: Option 9 — Discrete crack model

The interaction of each ply within the composite laminate plays a very important role and helps in determining the failure response of the component under the loading scenario. Delamination is considered

one of the most crucial damages for the impacted composites, as driven by the matrix cracking, bending cracks, and shear cracks [102]. Here, the*AUTOMATIC ONE WAY SURFACE TO SURFACE TIEBREAK* contact definition was used in this study. The formulation used to model the interaction between the plies of the laminates was based on *OPTION: 9* (Discrete Crack Model with power law or B-K damage models) as defined in the LS-Dyna environment. This model uses the mixed-mode traction–separation law based on the *MAT COHESIVE MIXED MODE* material model [132]. It includes the quadratic mixed mode delamination criterion and a damage formulation [73,79,82].

The total mixed-mode relative displacement δ_m is defined as:

$$\delta_m = \sqrt{\delta_I^2 + \delta_{II}^2} \tag{A.30}$$

$$\delta_I = \delta_3 \tag{A.31}$$

$$\delta_{II} = \sqrt{\delta_I^2 + \delta_2^2} \tag{A.32}$$

The mixed-mode damage initiation displacement δ^0 is given by:

$$\delta^0 = \delta_I^0 \delta_{II}^0 \sqrt{\frac{1+\beta^2}{(\delta_{II}^0)^2 + (\beta\delta_I^0)^2}} \tag{A.33}$$

$$\delta_I^0 = \frac{T}{EN} \tag{A.34}$$

$$\delta_{II}^0 = \frac{S}{ET} \tag{A.35}$$

$$\beta = \frac{\delta_{II}}{\delta_I} \tag{A.36}$$

So, the ultimate mixed-mode displacement δ^F (total failure) for the Benzeggagh–Kenane law is given as (1996):

$$\delta^F = \frac{2}{\delta^0(EN^{\gamma}\frac{1}{1+\beta^2} + ET^{\gamma}\frac{\beta^2}{1+\beta^2})}[GIC + (GIIC - GIC)(\frac{\beta^2 \times ET}{EN + \beta^2 \times ET})^{PARAM}] \tag{A.37}$$

Appendix B. Mesh sensitivity analysis

Mesh sensitivity analysis was conducted on the model utilizing MAT 55. Fig. B.1 illustrates the force–time histories for a 27.9 J impact using three distinct element sizes at the laminate-impactor contact area: 2 mm (coarse mesh), 0.5 mm (intermediate mesh), and 0.25 mm (fine mesh). The model coarse mesh tends to overestimate the peak impact force, while the difference in peak force between the intermediate and fine meshes is minimal. In the analysis, the model with a smaller mesh size exhibited lower stiffness, increased damage, and longer impact time duration, a common occurrence in such models due to strain localization [133]. To address mesh sensitivity in such a scenario, regularization methods are necessary to provide a correlation between element size and fracture energy or failure strain [26,70] which is not implemented in the definition of MAT 55 and MAT 162. Therefore, to avoid mesh sensitivity problems regularization of failure strain parameters is suggested when the element size of the model is changed. We implemented regulated failure strain parameters in the model following: $EFS_n = (L_o/L_n)EFS_o$, where L is the element length and subscripts n and o represent new and old elements, respectively. This resulted in outcomes that aligned more consistently with the results presented in Section 5.1, as shown in Fig. B.1. This adjustment effectively mitigated the issues typically associated with finer mesh sizes in impact simulations by providing a more consistent impact response curve.

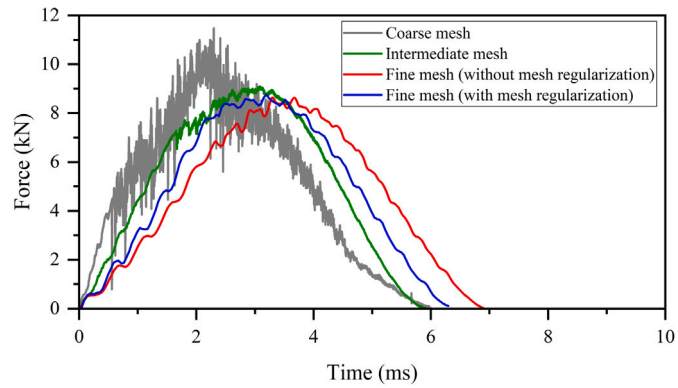

Fig. B.1. Mesh sensitivity analysis on a model with MAT 55 for impact energy of 27.9 J: Force–time histories for fine (with and without mesh regularization), intermediate, and coarse meshes.

References

[1] Y. Karsandik, B. Sabuncuoglu, B. Yildirim, V.V. Silberschmidt, Impact behavior of sandwich composites for aviation applications: A review, Compos. Struct. (2023) 116941.
[2] A. Syamsir, L.-W. Ean, M.R.M. Asyraf, A.B.M. Supian, E. Madenci, Y.O. Özkılıç, C. Aksoylu, Recent advances of GFRP composite cross arms in energy transmission tower: A short review on design improvements and mechanical properties, Materials 16 (7) (2023) 2778.
[3] S. Siengchin, A review on lightweight materials for defence applications: A present and future developments, Def. Technol. (2023).
[4] I. Sioutis, K. Tserpes, A literature review on crack arrest features for composite materials and composite joints with a focus on aerospace applications, Aerospace 10 (2) (2023) 137.
[5] X. Li, X. Zhang, R. Yan, L. Jia, Structural design and impact resistance of three-dimensional structure-reinforced flexible polymer composites, Polym. Adv. Technol. 34 (2) (2023) 506–519.
[6] L. Liu, Z. Yang, J. Ji, G. Chen, G. Luo, W. Chen, Development and experimental verification of a modified constitutive model for 3D orthogonal woven composite under bird impact, Compos. Struct. 303 (2023) 116305.
[7] L. Navrátil, N. Carrere, V. Le Saux, S. Leclercq, Y. Marco, On the ability of a viscoelastic model to predict the average cyclic energy dissipated by a 3D layer-to-layer composite, Compos. Struct. 303 (2023) 116264.
[8] J.N. Baucom, M.A. Zikry, A.M. Rajendran, Low-velocity impact damage accumulation in woven S2-glass composite systems, Compos. Sci. Technol. 66 (10) (2006) 1229–1238.
[9] C. Dong, H.A. Ranaweera-Jayawardena, I.J. Davies, Flexural properties of hybrid composites reinforced by S-2 glass and T700S carbon fibres, Composites B 43 (2) (2012) 573–581.
[10] A. Boukar, S. Corn, P.R. Slangen, P. Ienny, Finite element modelling of low velocity impact test applied to biaxial glass fiber reinforced laminate composites, Int. J. Impact Eng. 165 (March) (2022) 104218.
[11] G. Guillamet, A. Quintanas-Corominas, M. Rivero, G. Houzeaux, M. Vázquez, A. Turon, Application of the partial Dirichlet–Neumann contact algorithm to simulate low-velocity impact events on composite structures, Composites A (2023) 107424.
[12] S. Shah, P. Megat-Yusoff, S. Karuppanan, R. Choudhry, F. Ahmad, Z. Sajid, P. Gerard, K. Sharp, Performance comparison of resin-infused thermoplastic and thermoset 3D fabric composites under impact loading, Int. J. Mech. Sci. 189 (2021) 105984.
[13] R. Muhi, F. Najim, M.F. de Moura, The effect of hybridization on the GFRP behavior under high velocity impact, Composites B 40 (8) (2009) 798–803.
[14] A. Formisano, L. Boccarusso, M. Durante, A. Langella, Punch tool based out-of-plane shear behaviour of GFRP composites, Compos. Struct. 163 (2017) 325–330.
[15] Y. Ke, S. Huang, B. Sun, B. Gu, Investigation on mechanical properties and damage evolution of thermo-oxidative aged 3D angle-interlock woven composites under quasi-static tension, Eng. Fract. Mech. 282 (2023) 109204.
[16] V. Zhigun, E. Plume, S. Kristone, L. Krasnov, Method for determining the shear moduli of composite materials from experiments in the three-point transverse bending, Mech. Compos. Mater. (2023) 1–12.
[17] Z.-Q. Cheng, W. Tan, J.-J. Xiong, Progressive damage modelling and fatigue life prediction of plain-weave composite laminates with low-velocity impact damage, Compos. Struct. 273 (2021) 114262.
[18] Z. Cheng, J. Xiong, Progressive damage behaviors of woven composite laminates subjected to LVI, TAI and CAI, Chin. J. Aeronaut. 33 (10) (2020) 2807–2823.

[19] T.P. Sathishkumar, S. Satheeshkumar, J. Naveen, Glass fiber-reinforced polymer composites - A review, J. Reinf. Plast. Compos. 33 (13) (2014) 1258–1275.

[20] T. Huang, Y. Wang, G. Wang, Review of the mechanical properties of a 3D woven composite and its applications, Polym.-Plast. Technol. Eng. 57 (8) (2018) 740–756.

[21] H.A. Aisyah, M.T. Paridah, S.M. Sapuan, R.A. Ilyas, A. Khalina, N.M. Nurazzi, S.H. Lee, C.H. Lee, A comprehensive review on advanced sustainable woven natural fibre polymer composites, Polymers 13 (3) (2021) 1–45.

[22] M. Al-Furjan, L. Shan, X. Shen, M. Zarei, M. Hajmohammad, R. Kolahchi, A review on fabrication techniques and tensile properties of glass, carbon, and Kevlar fiber reinforced polymer composites, J. Mater. Res. Technol. 19 (2022) 2930–2959.

[23] M. Heidari-Rarani, M. Sayedain, Finite element modeling strategies for 2D and 3D delamination propagation in composite DCB specimens using VCCT, CZM and XFEM approaches, Theor. Appl. Fract. Mech. 103 (2019) 102246.

[24] L. Wan, Y. Sheng, E.D. McCarthy, D. Yang, A novel approach for 3D discrete element modelling the progressive delamination in unidirectional CFRP composites, Eng. Fract. Mech. 277 (2023) 108982.

[25] A. Aktaş, M. Aktaş, F. Turan, The effect of stacking sequence on the impact and post-impact behavior of woven/knit fabric glass/epoxy hybrid composites, Compos. Struct. 103 (2013) 119–135.

[26] H. Liu, B.G. Falzon, W. Tan, Experimental and numerical studies on the impact response of damage-tolerant hybrid unidirectional/woven carbon-fibre reinforced composite laminates, Composites B 136 (2018) 101–118.

[27] H. Liu, J. Liu, Y. Ding, Z.E. Hall, X. Kong, J. Zhou, B.R. Blackman, A.J. Kinloch, J.P. Dear, A three-dimensional elastic-plastic damage model for predicting the impact behaviour of fibre-reinforced polymer-matrix composites, Composites B 201 (2020) 108389.

[28] C. Bouvet, S. Rivallant, J.-J. Barrau, Low velocity impact modeling in composite laminates capturing permanent indentation, Compos. Sci. Technol. 72 (16) (2012) 1977–1988.

[29] X. Li, D. Ma, H. Liu, W. Tan, X. Gong, C. Zhang, Y. Li, Assessment of failure criteria and damage evolution methods for composite laminates under low-velocity impact, Compos. Struct. 207 (2019) 727–739.

[30] T. Mitrevski, I.H. Marshall, R. Thomson, The influence of impactor shape on the damage to composite laminates, Compos. Struct. 76 (1–2) (2006) 116–122.

[31] T. Mitrevski, I.H. Marshall, R. Thomson, R. Jones, B. Whittingham, The effect of impactor shape on the impact response of composite laminates, Compos. Struct. 67 (2) (2005) 139–148.

[32] M. Rezasefat, D. Ma, A.A. da Silva, C. Colombo, S.C. Amico, M. Giglio, A. Manes, Multi-criteria decision-making analysis and numerical simulation of the low-velocity impact response of inter-ply S2-glass/aramid woven fabric hybrid laminates, Compos. Struct. 312 (2023) 116867.

[33] E.-H. Kim, M.-S. Rim, I. Lee, T.-K. Hwang, Composite damage model based on continuum damage mechanics and low velocity impact analysis of composite plates, Compos. Struct. 95 (2013) 123–134.

[34] S.H. Khan, A.P. Sharma, Influence of metal/composite interface on the damage behavior and energy absorption mechanisms of FMLs against projectile impact, Def. Technol. 18 (3) (2022) 441–456.

[35] S. Tiwari, C.K. Hirwani, A.G. Barman, Dynamic behavior of hybrid composite shallow shell panel-FEM HOSDT and experimental approach, Eur. J. Mech. A Solids 97 (2023) 104772.

[36] B. Yang, Y. Chen, J. Lee, K. Fu, Y. Li, In-plane compression response of woven CFRP composite after low-velocity impact: Modelling and experiment, Thin-Walled Struct. 158 (June 2020) (2021) 107186.

[37] A. Rajaneesh, M. Bruyneel, Low-velocity impact and compression after impact modeling of composites using modified mesoscale model, Compos. Struct. 311 (2023) 116821.

[38] P. Ladevèze, O. Allix, J.-F. Deü, D. Lévêque, A mesomodel for localisation and damage computation in laminates, Comput. Methods Appl. Mech. Engrg. 183 (1–2) (2000) 105–122.

[39] J. Zhang, Y. Wang, Y. Wen, X. Dai, Y. Zhao, G. Fang, Energy dissipation mechanism of fiber metal laminate under low-velocity impact, Thin-Walled Struct. 183 (2023) 110355.

[40] J. Gebhardt, M. Schlamp, I. Ehrlich, S. Hiermaier, Low-velocity impact behavior of elliptic curved composite structures, Int. J. Impact Eng. (2023) 104663.

[41] H. Zhao, C. Li, Y. Fu, M.A. Oyarhossein, M. Habibi, H. Safarpour, Quasi-static indentation, low-velocity impact, and resonance responses of the laminated double-curved panel considering various boundary conditions, Thin-Walled Struct. 183 (2023) 110360.

[42] S. Xu, S. Zhang, W. Shen, X. huang, Y. Qiu, Y. Wu, Low-speed impact of glass/Kevlar hybrid composites: Experimental results and numerical verification, J. Compos. Mater. (2023) 00219983231183035.

[43] X. Zhou, W. Xu, H. Zhou, Y. Zhang, P. Wang, Z. Gu, Y. Li, Low-velocity impact properties of carbon fiber/ultrahigh molecular weight polyethylene fiber hybrid composites, Polym. Compos. (2023).

[44] Y. Yang, Q. Liang, H. Dou, M. Sun, K. Qian, D. Zhang, Low velocity impact failure mechanisms of carbon/UHMWPE 2.5 d woven hybrid composites via experimental and numerical methods, Compos. Struct. (2023) 117290.

[45] D. Chen, Q. Luo, M. Meng, Q. Li, G. Sun, Low velocity impact behavior of inter-layer hybrid composite laminates with carbon/glass/basalt fibres, Composites B 176 (2019) 107191.

[46] D.-K. Choi, S.-W. Byun, G.-H. Lee, S.-Y. Lee, J.-H. Roh, C.-J. Lee, Damage prediction of thick composite laminates subjected to low-velocity impact loads, Adv. Compos. Mater. 31 (6) (2022) 669–682.

[47] G.C. Jacob, J.M. Starbuck, J.F. Fellers, S. Simunovic, R.G. Boeman, Strain rate effects on the mechanical properties of polymer composite materials, J. Appl. Polym. Sci. 94 (1) (2004) 296–301.

[48] K. Wang, L. Zhao, H. Hong, J. Zhang, A strain-rate-dependent damage model for evaluating the low velocity impact induced damage of composite laminates, Compos. Struct. 201 (2018) 995–1003.

[49] M. Yang, A. Cui, X. Huang, Analysis of low velocity impact properties of basalt fiber composites considering strain rate effect, J. Strain Anal. Eng. Des. 58 (4) (2023) 257–269.

[50] L. Ma, F. Liu, D. Liu, Y. Liu, Review of strain rate effects of fiber-reinforced polymer composites, Polymers 13 (17) (2021) 2839.

[51] B. Liao, P. Liu, Finite element analysis of dynamic progressive failure of plastic composite laminates under low velocity impact, Compos. Struct. 159 (2017) 567–578.

[52] C.-F. Yen, Ballistic impact modeling of composite materials, in: Proceedings of the 7th International LS-DYNA Users Conference, Vol. 6, 2002, pp. 15–23.

[53] T. Pittie, K. Kartikeya, N. Bhatnagar, N.A. Krishnan, T. Senthil, S.D. Rajan, Building a predictive soft armor finite element model combining experiments, simulations, and machine learning, J. Compos. Mater. 57 (9) (2023) 1599–1615.

[54] Y. Kumar, M. Rezasefat, J.D. Hogan, Axial crushing of circular thin-walled specimens made of CFRP using progressive failure model (MAT54) in LS-Dyna, Mater. Today Proc. (2023).

[55] P. Feraboli, B. Wade, F. Deleo, M. Rassaian, M. Higgins, A. Byar, LS-DYNA MAT54 modeling of the axial crushing of a composite tape sinusoidal specimen, Composites A 42 (11) (2011) 1809–1825.

[56] K. Krishnan, S. Sockalingam, S. Bansal, S. Rajan, Numerical simulation of ceramic composite armor subjected to ballistic impact, Composites B 41 (8) (2010) 583–593.

[57] B. Berk, R. Karakuzu, A.K. Toksoy, An experimental and numerical investigation on ballistic performance of advanced composites, J. Compos. Mater. 51 (25) (2017) 3467–3480.

[58] N.N. Hussain, S.P. Regalla, Y.V.D. Rao, Techniques for correlation of drop weight impact testing and numerical simulation for composite GFRP crash boxes using Ls-Dyna, Int. J. Crashworthiness 27 (3) (2022) 700–716.

[59] J. Reiner, N. Zobeiry, R. Vaziri, A stacked sublaminate-based damage-plasticity model for simulating progressive damage in composite laminates under impact loading, Thin-Walled Struct. 156 (2020) 107009.

[60] J.B. Jordan, C.J. Naito, B.Z.G. Haque, Progressive damage modeling of plain weave E-glass/phenolic composites, Composites B 61 (2014) 315–323.

[61] A. Forghani, A. Poursartip, R. Vaziri, An orthotropic non-local approach to modeling intra-laminar damage progression in laminated composites, Int. J. Solids Struct. 180 (2019) 160–175.

[62] T.A. Rossi, K. Fayazbakhsh, Z. Fawaz, Application of LS-DYNA constitutive material model laws to simulate low velocity impact damage to composite plates, J. Aerosp. Eng. 33 (6) (2020).

[63] J.O. Hallquist, Livermore Software Technology Corporation (LSTC), LS-DYNA Keyword User's Manual Volume II: Material Models, Vol. II, (October) 2018, pp. 1–1619.

[64] G. Sun, D. Chen, G. Zhu, Q. Li, Lightweight hybrid materials and structures for energy absorption: A state-of-the-art review and outlook, Thin-Walled Struct. 172 (2022) 108760.

[65] A. Pandey, A. Upadhyay, K. Shukla, Multi-objective optimization of geometrical parameters of composite sandwich panels with an aluminum honeycomb core for an improved energy absorption, Mech. Compos. Mater. 59 (1) (2023) 45–64.

[66] Y. Gitiara, R. Barbaz-Isfahani, S. Saber-Samandari, M. Sadighi, Low-velocity impact behavior of incorporated GFRP composites with nanoclay and nanosilica in a corrosive environment: Experimental and numerical study, J. Compos. Mater. 55 (27) (2021) 3989–4010.

[67] S. Samlal, R. Santhanakrishnan, Low-velocity impact behavior of foam core sandwich panels with inter-ply and intra-ply carbon/Kevlar/epoxy hybrid face sheets, Polymers 14 (5) (2022) 1060.

[68] B.L. Sy, Z. Fawaz, H. Bougherara, Numerical simulation correlating the low velocity impact behaviour of flax/epoxy laminates, Composites A 126 (2019) 105582.

[69] S. Sridharan, M. Pankow, Performance evaluation of two progressive damage models for composite laminates under various speed impact loading, Int. J. Impact Eng. 143 (August 2019) (2020) 103615.

[70] M. Rezasefat, A. Gonzalez-Jimenez, M. Giglio, A. Manes, An evaluation of cuntze and puck inter fibre failure criteria in simulation of thin CFRP plates subjected to low velocity impact, Compos. Struct. 278 (2021) 114654.

[71] A. Vescovini, L. Balen, R. Scazzosi, A.A. da Silva, S.C. Amico, M. Giglio, A. Manes, Numerical investigation on the hybridization effect in inter-ply S2-glass and aramid woven composites subjected to ballistic impacts, Compos. Struct. 276 (2021) 114506.

[72] W. Ao, W. Zhuang, B. Xing, Q. Zhou, Y. Xia, Finite element method of a progressive intralaminar and interlaminar damage model for woven fibre laminated composites under low velocity impact, Mater. Des. 223 (2022) 111256.
[73] J.R. Xiao, B.A. Gama, J.W. Gillespie, Progressive damage and delamination in plain weave S-2 glass/SC-15 composites under quasi-static punch-shear loading, Compos. Struct. 78 (2) (2007) 182–196.
[74] A. Cherniaev, C. Butcher, J. Montesano, Predicting the axial crush response of CFRP tubes using three damage-based constitutive models, Thin-Walled Struct. 129 (2018) 349–364.
[75] A.A.X. da Silva, R. Scazzosi, A. Manes, S.C. Amico, High-velocity impact behavior of aramid/S2-glass interply hybrid laminates, Appl. Compos. Mater. 28 (6) (2021) 1899–1917.
[76] A.A.X. da Silva, J.A. Souza, A. Manes, S.C. Amico, In-plane Permeability and Mechanical Properties of R-Glass/Aramid Hybrid Composites, J. Mater. Eng. Perform. 29 (7) (2020) 4484–4492.
[77] F. Fulginiti, M. Rezasefat, A.X. Silva, S.C. Amico, M. Giglio, A. Manes, M. Rezasefat, A.X. Silva, S.C. Amico, M. Giglio, A. Manes, Experimental and numerical studies on the repeated low-velocity impact response and damage accumulation in woven S2-glass fibre / epoxy composites, Adv. Compos. Mater. 00 (00) (2023) 1–26.
[78] S. Shah, P. Megat-Yusoff, S. Karuppanan, R. Choudhry, F. Ahmad, Z. Sajid, P. Gerard, K. Sharp, Performance comparison of resin-infused thermoplastic and thermoset 3D fabric composites under impact loading, Int. J. Mech. Sci. 189 (2021) 105984.
[79] B.A. Gama, J.W. Gillespie, Finite element modeling of impact, damage evolution and penetration of thick-section composites, Int. J. Impact Eng. 38 (4) (2011) 181–197.
[80] F. Martínez-Hergueta, D. Ares, A. Ridruejo, J. Wiegand, N. Petrinic, Modelling the in-plane strain rate dependent behaviour of woven composites with special emphasis on the non-linear shear response, Compos. Struct. 210 (November 2018) (2019) 840–857.
[81] G. Perillo, J.K. Jørgensen, Numerical/Experimental Study of the Impact and Compression after Impact on GFRP Composite for Wind/Marine Applications, Procedia Eng. 167 (1877) (2016) 129–137.
[82] Livermore Software Technology Corporation (LSTC), Keyword User's Manual Volume 1, Vol. I, 2014, p. 2350.
[83] M. Loikkanen, G. Praveen, D. Powell, Simulation of ballistic impact on composite panels, in: 10th International LS-DYNA Users Conference (Impact Analysis), pp. 1–12.
[84] J. Schön, Coefficient of friction of composite delamination surfaces, Wear 237 (1) (2000) 77–89.
[85] A. Faggiani, B. Falzon, Predicting low-velocity impact damage on a stiffened composite panel, Composites A 41 (6) (2010) 737–749.
[86] H. Yin, L. Iannucci, An experimental and finite element investigation of compression-after-impact (CAI) behaviour of biaxial carbon fibre non-crimp-fabric (NCF) based composites, Compos. Struct. 281 (2022) 115057.
[87] L. Maio, E. Monaco, F. Ricci, L. Lecce, Simulation of low velocity impact on composite laminates with progressive failure analysis, Compos. Struct. 103 (2013) 75–85.
[88] L.E. Schwer, S.W. Key, T. Pucik, L.P. Bindeman, An assessment of the LS-DYNA hourglass formulations via the 3D patch test, in: 5th European LS-DYNA Users Conference, 2005.
[89] B. Berk, R. Karakuzu, B. Murat Icten, V. Arikan, Y. Arman, C. Atas, A. Goren, An experimental and numerical investigation on low velocity impact behavior of composite plates, J. Compos. Mater. 50 (25) (2016) 3551–3559.
[90] F.-k. Chang, K.-Y. Chang, Laminated composites containing stress concentrations, J. Compos. Mater. 21 (September) (1987) 834–855.
[91] S.W. Tsai, E.M. Wu, A general theory of strength for anisotropic materials, J. Compos. Mater. 5 (1) (1971) 58–80.
[92] A. Cherniaev, C. Butcher, J. Montesano, Predicting the axial crush response of CFRP tubes using three damage-based constitutive models, Thin-Walled Struct. 129 (April) (2018) 349–364.
[93] F.V. de Camargo, A. Pavlovic, E.C. Schenal, C. Fragassa, Explicit stacked-shell modelling of aged basalt fiber reinforced composites to low-velocity impact, Compos. Struct. 256 (2021) 113017.
[94] Z. Hashin, Failure criteria for unidirectional fiber composites, J. Appl. Mech. Trans. ASME 47 (2) (1980) 329–334.
[95] A. Matzenmiller, J. Lubliner, R.L. Taylor, A constitutive model for anisotropic damage in fiber-composites, Mech. Mater. 20 (2) (1995) 125–152.
[96] B.Z.G. Haque, A Progressive Composite Damage Model for Unidirectional and Woven Fabric Composites, Materials Science Corporation (MSC) and University of Delaware Center for Composite Materials (UD-CCM), 2017.
[97] M. Albayrak, M.O. Kaman, I. Bozkurt, Determination of Ls-dyna Mat 162 Material Input Parameters for Low Velocity Impact Analysis of Layered Composites, Paris France, 2022, pp. 17–18, Feb.
[98] F.V. de Camargo, A. Pavlovic, E.C. Schenal, C. Fragassa, Explicit stacked-shell modelling of aged basalt fiber reinforced composites to low-velocity impact, Compos. Struct. 256 (2021) 113017.
[99] J.B. Jordan, C.J. Naito, B.Z.G. Haque, Progressive damage modeling of plain weave E-glass/phenolic composites, Composites B 61 (2014) 315–323.
[100] B.A. Gama, J.-R. Xiao, M. Haque, C. Yen, J. Gillespie, Experimental and Numerical Investigations on Damage and Delamination in Thick Plain Weave S-2 Glass Composites Under Quasi-Static Punch Shear Loading, Center for Composite Materials, University of Delaware, 2004.
[101] L. Deka, Quasi-Static and Multi-Site High Velocity Impact Response of Composite Structures, The University of Alabama at Birmingham, 2008.
[102] S.N.A.B. Safri, M. Sultan, M. Jawaid, Damage analysis of glass fiber reinforced composites, in: Durability and Life Prediction in Biocomposites, Fibre-Reinforced Composites and Hybrid Composites, Elsevier, 2019, pp. 133–147.
[103] M. Rezasefat, S.C. Amico, M. Giglio, A. Manes, A numerical study on the influence of strain rate in finite-discrete element simulation of the perforation behaviour of woven composites, Polymers 14 (20) (2022) 4279.
[104] M. Rezasefat, A.A. da Silva, S.C. Amico, M. Giglio, A. Manes, Repeated impact behaviour of inter-ply hybrid aramid/S2-glass epoxy laminates, Thin-Walled Struct. 186 (2023) 110680.
[105] G. Kinvi-Dossou, N. Bonfoh, R.M. Boumbimba, Y. Koutsawa, F. Lachaud, A. Nyoungue, P. Gerard, A mesoscale modelling approach of glass fibre/Elium acrylic woven laminates for low velocity impact simulation, Compos. Struct. 252 (2020) 112671.
[106] E. Erbayrak, E.U. Yuncuoglu, Y. Kahraman, B.E. Gumus, An experimental and numerical determination on low-velocity impact response of hybrid composite laminate, Iran. J. Sci. Technol. Trans. Mech. Eng. 45 (2021) 665–681.
[107] M. Rezasefat, A. Gonzalez-Jimenez, D. Ma, A. Vescovini, L. Lomazzi, A.A. da Silva, S.C. Amico, A. Manes, Experimental study on the low-velocity impact response of inter-ply S2-glass/aramid woven fabric hybrid laminates, Thin-Walled Struct. 177 (2022) 109458.
[108] B. Vieille, V.M. Casado, C. Bouvet, About the impact behavior of woven-ply carbon fiber-reinforced thermoplastic-and thermosetting-composites: a comparative study, Compos. Struct. 101 (2013) 9–21.
[109] S. Shah, S. Karuppanan, P. Megat-Yusoff, Z. Sajid, Impact resistance and damage tolerance of fiber reinforced composites: A review, Compos. Struct. 217 (2019) 100–121.
[110] E. Zorer, O. Özdemir, N. Öztoprak, An experimental study on low velocity impact behavior of thermoplastic composites repaired by composite patches, J. Compos. Mater. 54 (28) (2020) 4515–4524.
[111] J. Baucom, M. Zikry, A. Rajendran, Low-velocity impact damage accumulation in woven S2-glass composite systems, Compos. Sci. Technol. 66 (10) (2006) 1229–1238.
[112] Livermore Software Technology Corporation (LSTC), LS-DYNA Keyword User's Manual Volume II Material Models, Vol. II, Livermore Software Technology Corporation Livermore, CA, USA, 2014.
[113] A. Maazoun, S. Matthys, R. Mourao, J. Vantomme, Numerical prediction of the dynamic response of prestressed concrete hollow core slabs under blast loading, in: 11th European LS-Dyna Conference, 2017, pp. 1–8.
[114] S. Mohseni-Mofidi, C. Bierwisch, Application of hourglass control to Eulerian smoothed particle hydrodynamics, Comput. Part. Mech. 8 (1) (2021) 51–67.
[115] C.-F. Yen, Ballistic impact modeling of composite materials, in: Proceedings of the 7th International LS-DYNA Users Conference, Vol. 6, 2002, pp. 15–23.
[116] S. Boria, Sensitivity analysis of material model parameters to reproduce crushing of composite tubes, J. Mater. Eng. Perform. 28 (6) (2019) 3267–3280.
[117] D. Ma, Á. González-Jiménez, M. Giglio, C.M. dos Santos Cougo, S.C. Amico, A. Manes, Multiscale modelling approach for simulating low velocity impact tests of aramid-epoxy composite with nanofillers, Eur. J. Mech. A Solids 90 (2021) 104286.
[118] B. Kazemianfar, M. Esmaeeli, M.R. Nami, Experimental investigation on response and failure modes of 2D and 3D woven composites under low velocity impact, J. Mater. Sci. 55 (3) (2020) 1069–1091.
[119] B. Kazemianfar, M.R. Nami, Influence of oblique low velocity impact on damage behavior of 2D and 3D woven composites: Experimental and numerical methods, Thin-Walled Struct. 167 (2021) 108253.
[120] F. Ahmad, F. Abbassi, M.K. Park, J.-W. Jung, J.-W. Hong, Finite element analysis for the evaluation of the low-velocity impact response of a composite plate, Adv. Compos. Mater. 28 (3) (2019) 271–285.
[121] A.K. Bandaru, S. Patel, Y. Sachan, R. Alagirusamy, N. Bhatnagar, S. Ahmad, Low velocity impact response of 3D angle-interlock Kevlar/basalt reinforced polypropylene composites, Mater. Des. 105 (2016) 323–332.
[122] W. Hufenbach, F.M. Ibraim, A. Langkamp, R. Böhm, A. Hornig, Charpy impact tests on composite structures–an experimental and numerical investigation, Compos. Sci. Technol. 68 (12) (2008) 2391–2400.
[123] D.-H. Kim, K.-H. Jung, I.-G. Lee, H.-J. Kim, H.-S. Kim, Three-dimensional progressive failure modeling of glass fiber reinforced thermoplastic composites for impact simulation, Compos. Struct. 176 (2017) 757–767.
[124] N. Naik, V.R. Kavala, High strain rate behavior of woven fabric composites under compressive loading, Mater. Sci. Eng. A 474 (1–2) (2008) 301–311.
[125] N.K. Naik, P. Yernamma, N.M. Thoram, R. Gadipatri, V.R. Kavala, High strain rate tensile behavior of woven fabric E-glass/epoxy composite, Polym. Test. 29 (1) (2010) 14–22.

[126] X. Ge, P. Zhang, F. Zhao, M. Liu, J. Liu, Y. Cheng, Experimental and numerical investigations on the dynamic response of woven carbon fiber reinforced thick composite laminates under low-velocity impact, Compos. Struct. 279 (2022) 114792.
[127] Z. Cheng, J. Xiong, Progressive damage behaviors of woven composite laminates subjected to LVI, TAI and CAI, Chin. J. Aeronaut. 33 (10) (2020) 2807–2823.
[128] H. Miao, Z. Wu, Z. Ying, X. Hu, The numerical and experimental investigation on low-velocity impact response of composite panels: Effect of fabric architecture, Compos. Struct. 227 (2019) 111343.
[129] M. Osborne, Single-Element Characterization of the LS-DYNA MAT54 Material Model, University of Washington, 2012.
[130] B. Haque, J.W. Gillespie Jr., Rate dependent progressive composite damage modeling using MAT162 in LS-DYNA, in: 13th International LS-DYNA USers Conference, 2014.
[131] J. Gillespie Jr., B. Gama, C. Cichanowski, J. Xiao, Interlaminar shear strength of plain weave S2-glass/SC79 composites subjected to out-of-plane high strain rate compressive loadings, Compos. Sci. Technol. 65 (11–12) (2005) 1891–1908.
[132] S. Marzi, O. Hesebeck, M. Brede, F. Kleiner, A rate-dependent, elasto-plastic cohesive zone mixed-mode model for crash analysis of adhesively bonded joints, in: 7th European LS-DYNA Conference, 2009.
[133] Z.P. Bažant, B.H. Oh, Crack band theory for fracture of concrete, Mat. Constr. 16 (1983) 155–177.